Publications of the Astronomical Society of the Pacific, 138:024405 (33pp), 2026 February https://doi.org/10.1088/1538-3873/ae406a

Chasing the Tides: Searching for Orbital Decay Signatures in Transit Timing Data and Tidal Models for 20 Hot Jupiters

Ahmet Cem Kutluay[1,2,3], Özgür Baştürk[3,4], Adrian J. Barker[5], Selçuk Yalçınkaya[2,3,4,6], John Southworth[1], Selim Osman Selam[3,4], Özlem Şimşir[2,3], Kaan Kaplan[7], Furkan Akar[2,3], İpek Aleyna Ertürk[2,3], Zeynep Zengin[8], Ebrar Akalın[8], Volkan Özsoy[8], Özdenur Yaldır[8], Dilara İçöz[8], Luigi Mancini[9,10], Burak Duru[2,3], Fatma Tezcan[11,12], Alkım Özfidan[2,3], Ushna Umar[13], Anaël Wünsche[14], Martin J. Burgdorf[15], Richard E. Cannon[16], Roberto Jose Figuera Jaimes[17,18,19,20], Tobias Cornelius Hinse[21], Vincent Okoth[16], Jeremy Tregloan-Reed[22], Elif Sıla Buğday[13], Utku Akdere[13], Yiğit Turan[23], Sinan Aliş[24], Cihan Tuğrul Tezcan[11], Fuat Korhan Yelkenci[24], and Selina Hajarat[13]

[1] Astrophysics Group, Keele University, Staffordshire, ST5 5BG, UK
[2] Ankara University, Graduate School of Natural & Applied Sciences, Astronomy & Space Sciences Department, Ziraat Mahallesi İrfan Baştuğ Caddesi, Dışkapı, TR-06110 Altındağ/Ankara, Türkiye
[3] Ankara University, Astronomy and Space Sciences Research and Application Center (Kreiken Observatory), İncek Blvd., TR-06837, Ahlatlıbel, Ankara, Türkiye
[4] Ankara University, Faculty of Science, Astronomy & Space Sciences Department, Tandoğan, TR-06100, Ankara, Türkiye
[5] School of Mathematics, University of Leeds, Leeds LS2 9JT, UK
[6] Astrobiology Research Unit, Université de Liège, Allée du 6 Août 19C, B-4000 Liége, Belgium
[7] Sivas Science and Technology University, Gültepe Neighborhood, Mecnun Otyakmaz Street No:1, Sivas, Türkiye
[8] Middle East Technical University, Physics Department, 06800, Ankara, Türkiye
[9] Department of Physics, University of Rome "Tor Vergata," Via della Ricerca Scientifica 1, 00133 Rome, Italy
[10] INAF—Turin Astrophysical Observatory, via Osservatorio 20, 10025, Pino Torinese, Italy
[11] Türkiye National Observatories, DAG, 25050, Erzurum, Türkiye
[12] Atatürk University, Astronomy and Astrophysics, Erzurum, Türkiye
[13] Department of Physics, Faculty of Science, Bilkent University, TR-06800 Ankara, Türkiye
[14] Baronnies Provençales Observatory, Hautes Alpes, Parc Naturel Regional des Baronnies Provençales, F-05150 Moydans, France
[15] Earth System Sciences, Atmospheric Science, University of Hamburg, Hamburg, Germany
[16] Institute for Astronomy, University of Edinburgh, Royal Observatory, Edinburgh EH9 3HJ, UK
[17] Instituto de Astronomía y Ciencias Planetarias, Universidad de Atacama, Copiapó 485, Copiapö, Chile
[18] Millennium Institute of Astrophysics MAS, Nuncio Monsenor Sotero Sanz 100, Of. 104, Providencia, Santiago, Chile
[19] Instituto de Astrofísica, Facultad de Física, Pontificia Universidad Católica de Chile, Av. Vicuña Mackenna 4860, 7820436, Macul, Santiago, Chile
[20] Centre for Exoplanet Science, SUPA, School of Physics & Astronomy, University of St Andrews, North Haugh, St Andrews KY16 9SS, UK
[21] University of Southern Denmark, Department of Physics, Chemistry and Pharmacy, SDU-Galaxy, Campusvej 55, 5230, Odense M, Denmark
[22] Centro de Astronomía, Universidad de Antofagasta, Av. Angamos 601, Antofagasta, Chile
[23] Department of Physics, Imperial College London, London, SW7 2AZ, UK
[24] Department of Astronomy and Space Sciences, Faculty of Science, Istanbul University, 34119 İstanbul, Türkiye

Received 2025 December 20; revised 2026 January 28; accepted 2026 February 2; published 2026 February 26

Abstract

In this work, we present a transit timing variation analysis for 20 hot Jupiter systems, which we interpret with theoretical tidal dissipation models. For the majority of the sample, we conclude that a constant orbital period model represents the timing data best. Only WASP-12 b, TrES-1 b and WASP-121 b exhibit a changing orbital period, according to the most up-to-date results. We updated the orbital decay rate of WASP-12 b to $\dot{P} = -29.4 \pm 4.0$ ms yr^{-1} and the corresponding stellar tidal quality factor to $Q'_* = 1.72 \pm 0.18 \times 10^5$. For TrES-1 b, the median quadratic model suggests a period decrease at a rate of -14.9 ± 0.6 ms yr^{-1}, but the corresponding $Q'_* = 570 \pm 60$ does not agree with the theoretical estimates, which suggest $Q'_* \sim 10^6$ due to internal gravity wave dissipation. Lastly, WASP-121 b exhibits orbital growth at a rate of 15.1 ± 0.8 ms yr^{-1}, and theoretical results support outward migration due to strong inertial wave dissipation.

Supplementary material for this article is available online

Unified Astronomy Thesaurus concepts: Exoplanets (498); Hot Jupiters (753); Transit timing variation method (1710); Tidal interaction (1699); Star-planet interactions (2177)

1. Introduction

Tidal interactions are key driving mechanism of orbital and rotational evolution in both binary stars and exoplanetary systems, especially for planets with short orbital periods. These interactions lead to a transfer of angular momentum between the planet and its host star via energy dissipation, leading to orbital circularization, tidal synchronization, or, in some cases, orbital decay (e.g. Hut 1980, 1981; Ogilvie 2014; Barker 2025). Circularization of hot Jupiters (hereafter HJs) is primarily driven by dissipation within the planet (e.g. Guillot et al. 1996; Lazovik et al. 2024; Penev 2026), while stellar tides mostly dominate orbital decay for planets orbiting faster than the stellar rotation. Once circularized, further tidal dissipation in the star continuously removes angular momentum from the orbit, causing close-in planets to migrate inward over long timescales (e.g. Essick & Weinberg 2016; Chernov et al. 2017; Barker 2020), such as the several Myr decay timescale inferred for WASP-12 b (e.g. Maciejewski et al. 2016; Patra et al. 2017; Kutluay et al. 2023).

HJs provide a natural laboratory for studying tidal theory in star-planet systems. Their short orbital periods ($P_{\text{orb}} < 10$ days; Wang et al. 2015) and proximity to their host stars enhance the magnitude of tidal forces. Two pieces of evidence indicating the efficiency of tides in these systems include: (1) the predominance of circular orbits among the shortest-period systems (e.g. Penev 2026); and (2) the relatively low velocity scatter of HJ host stars, which is an indicator that they represent a younger population potentially evolving further through tidally-driven inspiral (e.g. Hamer & Schlaufman 2019). In addition to that, direct observational evidence for orbital decay of HJs has been provided by recent JWST observations of ZTF SLRN-2020 (De et al. 2023; Lau et al. 2025).

A comprehensive picture of orbital decay comes from two complementary approaches. The orbital period of a planet changes as its orbit shrinks (or grows) as a result of angular momentum exchanges. Transit Timing Variations (TTVs) provide a powerful method for detecting variations in transit mid-times on the order of seconds to minutes over long timescales (Agol et al. 2005). Identifying such small deviations requires a long temporal baseline of transit observations (Patra et al. 2017; Winn 2019), as longer high-precision datasets increase sensitivity to gradual changes in the orbital period and improve model discrimination (see Equation (35) in Jackson et al. 2023). Even tiny TTV shifts accumulate over years, potentially providing measurable signatures of orbital decay. Once statistically significant changes in orbital period are detected, the efficiency of tidal dissipation in the host star can be estimated by constraining the modified tidal quality factor (Q'), defined as the ratio of the tidal potential energy stored (E_0) to the kinetic energy dissipated per oscillation period ($\oint - \dot{E}\, dt$) due to tidal interactions (e.g. Goldreich & Soter 1966; Ogilvie 2014):

$$Q' = \frac{3Q}{2k_2} = \frac{3}{2k_2} 2\pi E_0 \left(\oint - \dot{E}\, dt \right)^{-1}. \tag{1}$$

Here k_2 is the quadrupolar Love number, which measures the degree of central condensation of a body, and takes a small value $\lesssim 0.05$ for a solar-type star. We have incorporated it into the definition of the tidal quality factor, as it is Q' that appears in tidal evolutionary equations.

If the rate of orbital period change due to tidal interactions can be determined, the stellar tidal quality factor ($Q'_\star$) can also be calculated using observable parameters according to (e.g. Birkby et al. 2014; Patra et al. 2017; Wilkins et al. 2017; L. Mancini et al. 2022)

$$Q'_\star = -\frac{27}{2}\pi \left(\frac{M_p}{M_\star} \right) \left(\frac{a}{R_\star} \right)^{-5} \left(\frac{dP_{\text{orb}}}{dE} \right)^{-1} P_{\text{orb}}. \tag{2}$$

Here P_{orb} is the orbital period, a is the semi-major axis, M_{p} and $M_\star$ are the planet and star masses respectively, $R_\star$ is the stellar radius, and dP_{orb}/dE is the orbital period change per cycle.

This method constrains the tidal quality factor at a snapshot in time, but $Q'_\star$ is generally not constant and depends on stellar properties that change as the star evolves. Evolved main-sequence stars and subgiants tend to exhibit more efficient tidal dissipation, corresponding to lower $Q'_\star$ values (e.g. Mathis 2015; F. Gallet et al. 2017; Barker 2020; Esseldeurs et al. 2024). Secondly, tidal dissipation is not believed to be governed by a single, uniform mechanism. Instead, depending on the region of a star and stellar evolutionary phase, different mechanisms can contribute to dissipation with varying levels of efficiency (e.g. Barker 2020). Recognizing the variability in tidal dissipation mechanisms across different stellar regions and evolutionary stages prompts a deeper examination of the underlying physical processes, which include equilibrium tides, inertial waves, and internal gravity waves.

Equilibrium tides describe the large-scale quasi-hydrostatic deformation of a body. For a quadrupolar tide ($l = 2$, $m = 2$), this is a spheroidal bulge and its associated flow (Ogilvie 2014). In stellar convective zones, turbulent convection dissipates the flow's kinetic energy (e.g. Ogilvie & Lin 2007; Duguid et al. 2020). For HJ systems, equilibrium tides are unlikely to cause significant orbital decay during the main sequence, with ${Q_{\text{eq}}}' \gtrsim 10^8$ for 0.8–1.4 $M_\odot$ stars, giving orbital decay timescales $\gtrsim$100 Gyr, far exceeding stellar lifetimes (Penev & Sasselov 2011; Barker 2020).

Inertial waves (IW) are excited when the tidal forcing frequency lies in $[-2\Omega, 2\Omega]$, where Ω is the stellar rotation rate (e.g. Ogilvie & Lin 2007; Ogilvie 2014; Astoul & Barker 2023). Restored by Coriolis forces, they propagate through the convective envelope and are most relevant in low-mass stars with deep convection zones. In HJ systems, IW rarely produce significant orbital decay during the main sequence, as the frequency condition is usually not satisfied for their excitation, though it is more likely to be satisfied in young or tidally spun-up stars. The resulting tidal quality factors span $Q'_\star \sim 10^7$–$10^{12}(P_{\rm rot}/10{\rm d})^2$ for 1.0–1.6 $M_\odot$ stars (where $P_{\rm rot} = 2\pi/\Omega$ is the stellar rotation period), indicating modestly efficient to inefficient dissipation. As stars evolve into subgiants, the expanding convective envelope and contracting radiative core enhance tidal dissipation, enabling IW excitation with $Q'_\star \sim 10^4$–$10^5(P_{\rm rot}/10{\rm days})^2$ (Barker 2020).

Internal gravity waves (IGW) are generated by tidal forces at the convective–radiative interface (e.g. Zahn 1975, 1977) and are restored by buoyancy forces. They propagate toward the stellar core, where they can amplify and break, leading to efficient dissipation (e.g. Goodman & Dickson 1998; Ogilvie & Lin 2007; Barker & Ogilvie 2010; Barker 2011; Weinberg et al. 2012). The efficiency of this process depends on the wave amplitude (see Equation 47 in Barker 2020). In particular, once a critical amplitude is exceeded, wave breaking produces efficient dissipation with a tidal quality factor $Q'_\star \sim 10^5(P_{\rm tide}/0.5{\rm day})^{8/3}$ (where $P_{\rm tide}$ is the tidal period) in main-sequence stars (Barker & Ogilvie 2010; Barker 2011). This critical amplitude can be interpreted in terms of a critical planetary mass (Equation (50) in Barker 2020), linking IGW breaking directly to planetary properties.

Several studies have highlighted the importance of IGWs for the orbital evolution of planetary systems (e.g. Chernov et al. 2017; Weinberg et al. 2017; Barker 2020; Ahuir et al. 2021; Ma & Fuller 2021; Guo et al. 2023), especially for host stars near the end of the main sequence, when short-period HJs are expected to be engulfed as their stars evolve (Hamer & Schlaufman 2019, 2020; Mustill et al. 2021; Weinberg et al. 2024).

An alternative mechanism for energy dissipation and outward propagation has been proposed for F-type stars with masses 1.2–1.6 $M_\odot$. In this scenario, IGWs propagating toward the core can be converted into magnetic waves by the strong magnetic field generated by the convective-core dynamo, provided the field is sufficiently strong (Duguid et al. 2024).

Formulas to simply evaluate the dissipation caused by each of these mechanisms are available (e.g. Barker 2020). The modified tidal quality factor for inertial waves can be obtained by

$$\frac{1}{\left\langle Q'_{\rm IW}\right\rangle} = \frac{32\pi^2 G}{3(2l+1)R^{2l+1}|A|^2}(E_l + E_{l-1} + E_{l+1}), \tag{3}$$

where E_l, E_{l-1} and E_{l+1} are parameters directly calculated from stellar evolution models, as described in Equations (31), (32) and (33) of Barker (2020). It should be noted that this formalism follows the frequency-averaged dissipation of inertial waves proposed by (Ogilvie 2013). The modified tidal quality factor for IGWs is:

$$\frac{1}{Q'_{\rm IGW}} = \frac{2\left[\Gamma\left(\frac{1}{3}\right)\right]^2}{3^{1/3}(2l+1)(l(l+1))^{4/3}}\frac{R}{GM_\star^2}\mathcal{G}|\omega|^{8/3}, \tag{4}$$

where the quantity $\mathcal{G}$ represents a combination of stellar structure parameters that characterize the properties of the radiative-convective boundary in a given stellar model (Equation 42 from Barker 2020) and $\omega = 2(\Omega_o - \Omega_s) = 2\pi/P_{\rm tide}$ is the tidal frequency for a circular, aligned orbit. We do not provide a formulation for equilibrium tides as they are less important than IWs and IGWs for HJs based on our current theoretical understanding.

If all or a combination of these processes operate, their effects can be summed via (Lazovik 2021)

$$\frac{1}{Q'} = \frac{1}{Q'_{\rm eq}} + \frac{1}{Q'_{\rm IW}} + \frac{1}{Q'_{\rm IGW}}. \tag{5}$$

The resulting dissipation from tidal forcing can leave a detectable signature in the orbital period variations observed through TTV analysis, providing insights into the stellar evolutionary phase, internal structure, and the timescales of orbital evolution.

Numerous studies have suggested that orbital decay signals can be detected observationally. As an example, the orbital decay of WASP-18 b was predicted to have become observable within a decade, with a reported decay timescale of 1×10^6 yr assuming $Q'_\star = 10^6$ (Hellier et al. 2009), though this has not been detected to date (e.g. Wilkins et al. 2017). Similarly, Penev et al. (2016) proposed that HATS-18 b should have undergone orbital decay due to stellar tidal dissipation, a claim later reinforced by Penev et al. (2018), who found $\log Q'_\star = 7.18^{+0.205}_{-0.173}$ (but see also Southworth et al. 2022). Additional cases include KELT-16 b (Maciejewski et al. 2018b; L. Mancini et al. 2022; Harre et al. 2023; Alvarado et al. 2024), WASP-19 b (Korth & Parviainen 2023; Biswas et al. 2024), WASP-4 b (Southworth et al. 2009a; Bouma et al. 2019; Turner et al. 2022; Baştürk et al. 2025), and WASP-43 b (Hellier et al. 2011; Hoyer et al. 2016), all suggesting observable orbital decay signatures.

With this study, our aim is to investigate the potential orbital decay of 20 HJs through TTV analysis, supported by theoretical predictions of tidal dissipation from stellar models. The systems we study are: CoRoT-2, HAT-P-23, HATS-18, KELT-9, KELT-16, Qatar-1, Qatar-4, TOI-2109, TOI-1937 A, TrES-1, WASP-3, WASP-12, WASP-19, WASP-46, WASP-87, WASP-103, WASP-114, WASP-121, WASP-122 (KELT-14) and WASP-167.

The remainder of this paper is organized as follows. In Section 2, we describe our target selection strategy. Section 3 presents the observational data and outlines the data reduction procedures. Section 4 discusses the methodology we employ in our analysis and the system-by-system results. Section 5 discusses our results further and finally, Section 6 summarizes our main conclusions.

2. Target Selection

The efficiency of tidal interactions depends strongly on fundamental system parameters, such as the stellar and planetary masses ($M_\star$ and M_p), stellar radius ($R_\star$) and the orbital semi-major axis (a). These dependencies are partly encapsulated in the modified tidal quality factor (Equation (2)). Moreover, as shown in Equations (3) and (4), the efficiency of tidal dissipation exhibits a steep dependence on the stellar radius, scaling as $R_\star^5$ in the quadrupolar ($l = 2$) case, which underscores the dominant role of stellar structure and stellar evolutionary phase in tidal energy dissipation. Even for $Q'_\star=$ const, independent of radius, tidal timescales tend to depend on stellar radius to a strong power, as we will show later with Equations (6) and (7).

When selecting systems that are most likely to exhibit observable orbital decay due to tidal effects, we prioritize the physical parameters mentioned above, which naturally lead us to focus on close-in giant planets orbiting solar-like stars (with $P_\mathrm{orb} \lesssim 2$ days)—particularly those approaching the end of their main-sequence lifetimes, as IWs and IGWs tend to become more efficient as their host stars evolve (for fixed P_rot and P_tide).

In this context, we employed two dimensionless metrics to estimate the relative strength of tidal interactions and their long-term dynamical effects, and thereby to select our best candidate systems. These were originally proposed by Siverd et al. (2012) and are defined as follows:

$$\tau_a \equiv \left(\frac{M_\star}{M_\mathrm{p}}\right)\left(\frac{a}{R_\star}\right)^5, \qquad (6)$$

and

$$\tau_{\omega_\star} \equiv \left(\frac{M_\star}{M_\mathrm{p}}\right)^2\left(\frac{a}{R_\star}\right)^3. \qquad (7)$$

Note that these are dimensionless quantities and are not timescales themselves. If we adopt a constant time-lag tidal model (Hut 1981; Matsumura et al. 2010) and assume a circular ($e = 0$), aligned orbit (the angle between the axes of stellar rotation and planetary orbit, $\lambda = 0$) around a slowly rotating star, the characteristic timescale of orbital decay to within an O(1) factor (that we omit here and depends on the power of a in the expression for $\dot{a}$) is $t_\mathrm{decay} \equiv a/|\dot{a}| = (12\pi)^{-1} Q'_\star \tau_a P_\mathrm{orb}$ and the timescale for the host star to be synchronized with its orbiting planet is $t_\mathrm{sync} \equiv \omega_\star/|\dot{\omega}_\star| \propto Q'_\star \tau_{\omega_\star} P_\mathrm{orb}$ (Matsumura et al. 2010). Hence τ_a and $\tau_{\omega_\star}$ are good measures of the relative strengths of tidal interactions, although they do not incorporate the variation in $Q'_\star$.

As an example, Siverd et al. (2012) adopted a stellar tidal quality factor of $Q'_\star = 10^8$, an orbital period $P_\mathrm{orb} \approx 1$ day for KELT-1, and found $\tau_a = 3 \times 10^4$, yielding an orbital decay timescale $t_\mathrm{decay} \approx 0.3$ Gyr. For the present study, to select candidate systems with potentially faster orbital decay (possibly due to IGWs, but not restricted to this mechanism), we fix $Q'_\star = 10^5$ and $P_\mathrm{orb} \approx 1$ day.

We focus on systems whose decay timescales are <500 Myr. To ensure unit consistency, the orbital period is converted from days to years, leading to $\tau_a = 12\pi \times t_\mathrm{decay}/Q'_\star \times 365.25$. Therefore, for the decay timescale range considered, τ_a needs to satisfy

$$\log_{10} \tau_a \lessapprox 7.$$

Similarly, for the spin synchronization timescale, we arbitrarily take our timescale range as 0–500 Myr ($t_\mathrm{decay} = t_\mathrm{sync}$). This gives $\tau_{\omega_\star} = 12\pi\tau_a$. Thus, we also focus on systems with

$$\log_{10} \tau_{\omega_\star} \lessapprox 8.5.$$

Based on these two criteria and a limit of $P_\mathrm{orb} \lesssim 2$ days, we first selected 19 HJ systems from the NASA Exoplanet Archive (Christiansen et al. 2025) and TEPCat (Southworth 2011) (both accessed on 2023 July 10) as potential candidates for exhibiting orbital decay behavior within the suggested timescale ranges. Figure 1 presents the distribution of all selected systems within the corresponding parameter space.

In contrast to most of the selected systems, TrES-1 does not lie in the region of the shortest predicted orbital-decay timescales. However, TTV analyses (e.g. Hagey et al. 2022; Adams et al. 2024) indicate a significant period decrease for TrES-1 b, suggesting that it remains a strong orbital-decay candidate despite its location in parameter space. Moreover, Jackson et al. (2023) showed that the ΔBIC in favor of an orbital decay model is expected to exceed the statistically decisive threshold (ΔBIC > 50) within the next few years. We therefore consider TrES-1 b a noteworthy target for continued monitoring and include it in our sample, especially because the system has been observed for more than 20 yr (Figure 4).

While KELT-9 stands out as an extreme case with its high temperature and stellar mass (see Table 1), placing it outside the typical spectral range of our sample, it was retained because it falls within the relevant region of the parameter space for which we could plausibly detect orbital decay. In addition, previous studies (Ivshina & Winn 2022; Harre et al. 2023) investigated the potential orbital period variation of KELT-9 b, hypothesizing that it may exhibit signs of orbital decay; however, no statistically significant evidence supporting this was found.

Despite some individual peculiarities, TrES-1 and KELT-9 were included in our sample, yielding 20 HJ systems for further analysis. All parameters used throughout the study are listed in Table 1. Some systems meeting our selection criteria

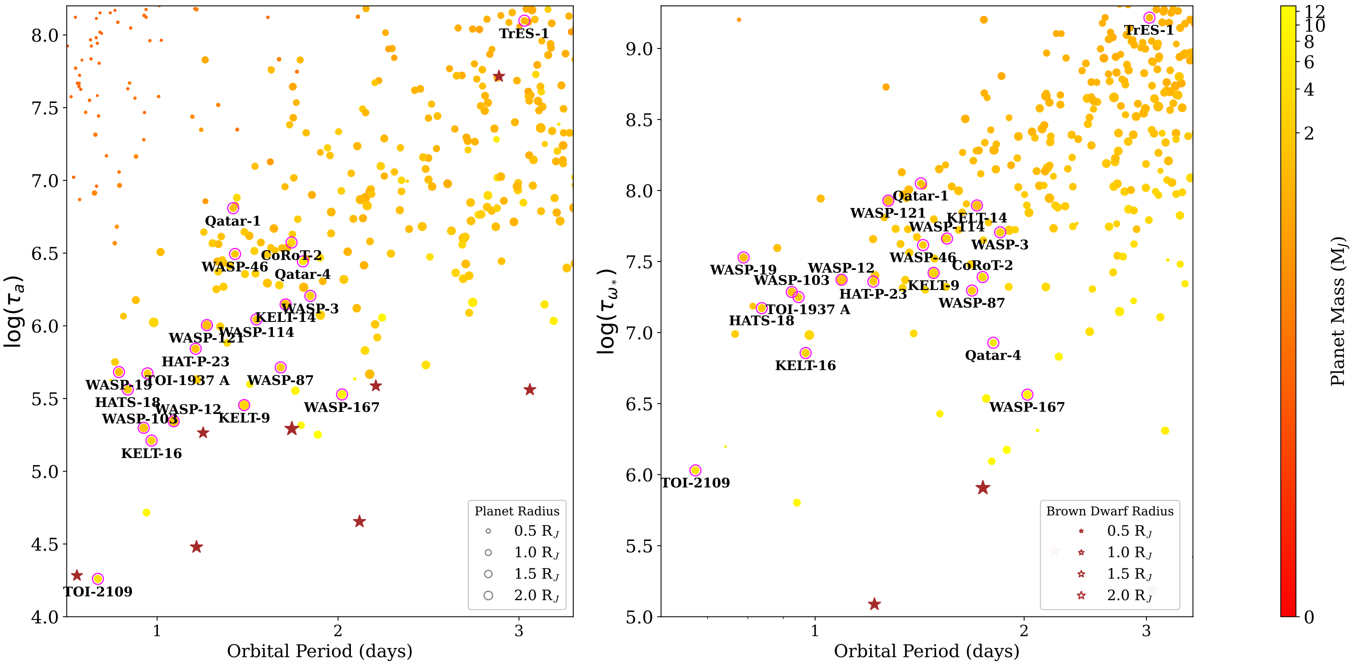

Figure 1. Orbital period versus the selection criteria parameters τ_a and $\tau_{\omega_\star}$ for objects from NASA Exoplanet Archive and TEPCat. The symbol size is proportional to the planetary (or brown dwarf) radius, while the color scale represents the planetary mass. The systems analyzed in this study are highlighted and labeled.

were excluded because reliable transit timing measurements or continuous coverage were unavailable for both space-borne and ground-based sources. These targets may be suitable for future studies with higher-cadence or longer-baseline monitoring, including HIP-65A b (Nielsen et al. 2020; Griffiths et al. 2026), CoRoT-14 b (Tingley et al. 2011), and HATS-70 b (Zhou et al. 2019).

3. Data and Reduction

3.1. Observations

3.1.1. TUG100 Observations

We used the T100 telescope at the Bakırlıtepe Campus of the Türkiye National Observatories, over nine nights to observe four of our targets (see Table 2). The T100 was equipped with a SI 1100 CCD camera with a field of view (FoV) of $20' \times 20'$ sampled at $0.29''\,\mathrm{px}^{-1}$. We defocussed the telescope to improve the data quality (Southworth et al. 2009b; Baştürk et al. 2015) and chose exposure times which gave the best signal-to-noise ratio (SNR) for each target.

3.1.2. AUKR T80 Observations

We observed seven targets during 10 nights with the T80 (Prof. Dr. Berahitdin Albayrak Telescope) at the Ankara University Kreiken Observatory. The CCD gave a FoV of $11\farcm84 \times 11\farcm84$ at $0\farcs69\,\mathrm{px}^{-1}$. We used an SDSS g', r', i' or z' filter, a slight defocussing, and exposure times that gave ≈50 points during each transit.

3.1.3. ATA050 Observations

We observed a transit of Qatar-1 during one night using the ATA050 telescope, at Türkiye National Observatories in Erzurum, Türkiye. The Apogee Alta U230 CCD camera gave a large FoV sampled at $2\farcs77\,\mathrm{px}^{-1}$. We used the Cousins R band and an exposure time of 110 s.

3.1.4. IST60 Observations

We observed three transits with the IST60 telescope at the Istanbul University Observatory (IUGUAM), at the Çanakkale Onsekiz Mart University Ulupınar Observatory, Türkiye. The Andor iXon Ultra 888 CCD camera had a FoV of $9\farcm6 \times 9\farcm6$ at $2\farcs56\,\mathrm{px}^{-1}$.

3.1.5. CDK20 and ODK20 Observations

Two transits of HATS-18 b were observed during 2 nights using a 50 cm CDK telescope (CDK20 in Table 2), which is located at the El Sauce Observatory (UAI code X02) in Chile but remotely controlled from France. A luminance filter was used to maximize the SNR. Four transits of WASP-19 were observed using a 50 cm ODK telescope (ODK20 in Table 2), a Moravian G4 16K CCD camera giving $0\farcs53\,\mathrm{px}^{-1}$, and an R filter. The reduction of these data was performed using the Muniwin program from the photometry software package C-Munipack (Hroch 2014).

Table 1

Fundamental Stellar and Planetary Parameters for Selected HJ Systems

System	$T_{\rm eff}$ (K)	Age (Gyr)	$M_\star$ ($M_\odot$)	$R_\star$ ($R_\odot$)	$P_{\rm orb}$ (days)	$M_{\rm p}$ ($M_{\rm J}$)	$a/R_\star$	$\log(\tau_a)$	$\log(\tau_{\omega_\star})$	Ref.
CoRoT-2	5625 ± 120	$2.7^{+3.2}_{-2.7}$	0.970 ± 0.060	0.902 ± 0.018	1.74299673(31)	$3.30^{+0.19}_{-0.18}$	6.70 ± 0.19	6.573	7.391	1,2
HAT-P-23	5905 ± 80	4 ± 1	1.130 ± 0.035	1.203 ± 0.074	1.21288287(17)	1.97 ± 0.12	4.15 ± 0.26	5.842	7.359	1
HATS-18	5600 ± 120	4.2 ± 2.2	1.037 ± 0.047	$1.020^{+0.057}_{-0.031}$	0.83784340(47)	1.980 ± 0.077	$3.71^{+0.11}_{-0.22}$	5.562	7.172	3
KELT-9	10170 ± 450	0.3	$2.52^{+0.25}_{-0.20}$	$2.362^{+0.075}_{-0.063}$	1.4811235(11)	2.88 ± 0.84	3.153 ± 0.011	5.455	7.420	4
KELT-16	6236 ± 54	3.1 ± 0.3	$1.211^{+0.043}_{-0.046}$	$1.360^{+0.064}_{-0.053}$	0.9689951(24)	$2.75^{+0.16}_{-0.15}$	$3.23^{+0.12}_{-0.13}$	5.211	6.856	5
Qatar-1	4910 ± 100	$11.60^{+0.60}_{-4.70}$	0.850 ± 0.030	0.800 ± 0.050	1.42002420(22)	$1.294^{+0.052}_{-0.049}$	$6.247^{+0.067}_{-0.065}$	6.809	8.05	1,7
Qatar-4	5215 ± 50	0.17 ± 0.01	0.896 ± 0.048	0.849 ± 0.063	1.8053663(15)	6.10 ± 0.54	7.11 ± 0.48	6.443	6.928	8,9
TOI-2109	6540 ± 160	$1.77^{+0.88}_{-0.68}$	1.453 ± 0.074	$1.698^{+0.062}_{-0.057}$	0.672474140(28)	5.02 ± 0.75	2.268 ± 0.021	4.26	6.03	10
TOI-1937 A	5814^{+91}_{-93}	$3.6^{+3.1}_{-2.3}$	$1.072^{+0.059}_{-0.064}$	$1.080^{+0.025}_{-0.024}$	0.94667944(47)	$2.01^{+0.17}_{-0.16}$	$3.85^{+0.09}_{-0.10}$	5.673	7.25	11
TrES-1	5230 ± 50	$3.7^{+3.4}_{-2.8}$	$0.878^{+0.038}_{-0.040}$	$0.807^{+0.017}_{-0.016}$	3.03006973(18)	$0.752^{+0.047}_{-0.046}$	$10.52^{+0.02}_{-0.18}$	8.098	9.217	1,12
WASP-3	6400 ± 100	2.1 ± 1.2	1.260 ± 0.100	1.366 ± 0.044	1.84683510(40)	1.89 ± 0.12	5.18 ± 0.35	6.206	7.706	1,23
WASP-12	6360^{+130}_{-140}	3.05 ± 0.32	$1.434^{+0.110}_{-0.090}$	$1.657^{+0.046}_{-0.044}$	1.09142030(14)	$1.470^{+0.076}_{-0.069}$	$3.039^{+0.034}_{-0.033}$	5.344	7.372	1,7
WASP-19	5616^{+66}_{-65}	$6.40^{+4.10}_{-3.50}$	$0.965^{+0.091}_{-0.095}$	$1.006^{+0.031}_{-0.034}$	0.78883852(82)	$1.154^{+0.078}_{-0.080}$	$3.533^{+0.048}_{-0.052}$	5.682	7.529	1,13
WASP-46	5600 ± 150	$9.60^{+3.40}_{-4.20}$	0.828 ± 0.067	0.858 ± 0.024	1.43036763(93)	1.91 ± 0.13	$5.851^{+0.038}_{-0.037}$	6.494	7.616	1,15,25
WASP-87	6450 ± 120	$\cdots$	1.204 ± 0.093	1.627 ± 0.062	1.6827950(19)	2.18 ± 0.15	$3.89^{+0.49}_{-0.42}$	5.714	7.296	16,17,18
WASP-103	6110 ± 160	4 ± 1	$1.220^{+0.039}_{-0.036}$	$1.220^{+0.039}_{-0.036}$	0.925542(19)	1.490 ± 0.088	$2.978^{+0.050}_{-0.096}$	5.299	7.286	19
WASP-114	5940 ± 140	$4.3^{+1.4}_{-1.3}$	1.289 ± 0.053	1.43 ± 0.06	1.54877430(120)	1.769 ± 0.064	4.29 ± 0.11	6.044	7.662	18,20
WASP-121	6459 ± 140	1.5 ± 1.0	$1.353^{+0.080}_{-0.079}$	1.458 ± 0.030	1.27492550(25)	$1.183^{+0.064}_{-0.062}$	$3.754^{+0.023}_{-0.028}$	6.005	7.929	21
WASP-122	5720 ± 130	5.11 ± 0.80	1.239 ± 0.039	1.52 ± 0.03	1.71005328(14)	1.284 ± 0.032	4.248 ± 0.072	6.147	7.895	18,22
WASP-167	7000 ± 250	$1.29^{+0.36}_{-0.27}$	1.59 ± 0.08	1.79 ± 0.05	2.0219596(6)	< 8	$4.23^{+0.08}_{-0.07}$	5.528	6.563	18,24

References: 1. Bonomo et al. (2017), 2. Bruno et al. (2016), 3. Penev et al. (2016), 4. Gaudi et al. (2017), 5. Oberst et al. (2017), 6. Chontos et al. (2019), 7. Collins et al. (2017a), 8. Alsubai et al. (2017), 9. Ivshina & Winn (2022), 10. Wong et al. (2021), 11. Yee et al. (2023), 12. Torres et al. (2008), 13. Cortés-Zuleta et al. (2020), 14. Esposito et al. (2017), 15. Ciceri et al. (2016), 16. Anderson et al. (2014), 17. Addison et al. (2016), 18. Kokori et al. (2023), 19. Gillon et al. (2014), 20. Barros et al. (2016), 21. Delrez et al. (2016), 22. Turner et al. (2016), 23. Stassun et al. (2017), 24. Temple et al. (2017), 25. Leonardi et al. (2024).

Table 2
Summary of the Observations

System	Date (yyyy-mm-dd)	Instrument	N_f	Filter	T_{exp} (s)	PNR (ppt)	β	Scatter (mmag)	Airmass
HAT-P-23	2025-07-12	T100	206	*V*	50	2.203	1.772	2.55	4.06 → 1.03
HATS-18	2024-05-08	CDK20	92	*L*	120	3.216	2.062	4.77	1.00 → 1.44
HATS-18	2024-05-29	CDK20	87	*L*	120	2.983	1.559	4.62	1.01 → 1.50
Qatar-1	2014-08-17	T100	64	*R*	120	0.678	1.554	1.00	1.23 → 1.13
Qatar-1	2019-10-30[a]	T100	161	*R*	90	1.071	2.767	1.35	1.14 → 1.79
Qatar-1	2020-03-07	T100	147	*R*	75	2.773	1.803	3.10	2.74 → 1.49
Qatar-1	2020-07-03	T100	110	*R*	100	1.453	1.370	1.91	1.45 → 1.14
Qatar-1	2020-08-23	IST60	104	*R*	120	4.172	1.876	5.55	1.17 → 1.68
Qatar-1	2020-09-19	IST60	84	*R*	110	3.699	1.239	4.89	1.31 → 1.91
Qatar-1	2020-10-02	T100	101	*R*	100	1.892	1.770	2.54	1.14 → 1.27
Qatar-1	2020-10-09	T100	70	*R*	120	1.122	1.332	1.61	1.26 → 1.75
Qatar-1	2020-05-10	ATA050	121	*R*	110	2.799	2.115	3.55	1.98 → 1.24
Qatar-1	2025-03-10	T80	202	SDSS-r'	60	3.144	1.402	3.05	2.29 → 1.35
Qatar-1	2025-06-09	T80	126	SDSS-g'	90	3.229	1.099	3.67	2.02 → 1.32
Qatar-4	2022-11-01	T80	125	SDSS-r'	110	2.274	1.698	2.88	1.08 → 2.11
TOI-2109	2023-05-01[b]	T80	81	SDSS-g'	120	1.243	1.039	1.73	1.82 → 1.11
TOI-2109	2024-06-27[c]	T100	204	SDSS-z'	25	2.491	1.347	2.50	1.09 → 1.06 → 1.35
TOI-2109	2024-07-01[a,b]	T80	133	SDSS-z'	105	1.832	3.370	2.45	1.09 → 1.12
TrES-1	2013-10-02	Loiano 1.5m	146	SDSS-r’	100	0.515	1.802	6.74	1.00 → 1.96
WASP-3	2020-08-31	IST60	81	R	75	2.860	2.184	4.66	1.01 → 1.59
WASP-3	2022-07-06	T80	220	SDSS-r'	60	0.716	0.895	0.68	1.00 → 1.41
WASP-3	2022-07-19	T80	230	SDSS-r'	60	1.167	1.859	1.12	1.01 → 1.29
WASP-12	2025-02-02	T100	107	SDSS-g'	120	1.312	1.839	2.02	1.15 → 1.00 → 1.23
WASP-12	2025-03-10	T80	222	SDSS-i'	75	1.526	1.745	1.59	1.08 → 2.45
WASP-19	2013-02-15	NTT	55	SDSS-r'	120	1.932	0.240	0.48	1.55 → 1.80 → 1.53
WASP-19	2013-02-16	NTT	67	SDSS-r'	120	2.220	0.278	0.55	1.68 → 1.05
WASP-19	2013-02-18[a]	NTT	63	SDSS-r'	120	2.582	0.275	0.55	1.04 → 1.94
WASP-19	2025-01-31[c]	ODK20	86	R	120	2.439	1.528	3.72	1.88 → 1.05
WASP-19	2025-03-27	ODK20	71	R	120	2.029	2.073	3.42	1.07 → 1.04 → 1.23
WASP-19	2025-04-07	ODK20	88	R	120	1.798	1.838	2.73	1.04 → 1.72
WASP-19	2025-04-11[c]	ODK20	61	R	120	2.115	1.408	3.19	1.04 → 1.32
WASP-19	2025-04-22	Danish 1.54m	259	R	30	1.692	0.884	1.33	1.09 → 1.96
WASP-19	2025-05-07	Danish 1.54m	143	I	80	1.675	2.380	1.96	1.12 → 2.48
WASP-19	2025-05-11	Danish 1.54m	323	I	20	2.164	1.651	1.49	1.08 → 1.65
WASP-103	2022-07-04	Danish 1.54m	153	R	100	0.490	2.175	0.63	1.39 → 1.24 → 2.24
WASP-103	2025-07-05	T80	534	SDSS-g'	25	1.689	1.936	1.87	1.18 → 2.25
WASP-114	2016-08-14	CAHA	163	R$_c$	120	1.944	0.789	1.09	1.30 → 1.12 → 1.98
WASP-114	2020-08-26	T80	111	SDSS-r'/SDSS-i'	150	1.270	2.072	1.98	1.17 → 1.14 → 2.27
WASP-121	2016-12-12	GROND	238	SDSS-g'	40/50/60	0.581	1.677	6.28	1.73 → 1.01 → 1.04
WASP-121	2016-12-12	GROND	238	SDSS-i'	40/50/60	0.807	2.035	8.70	1.73 → 1.01 → 1.04
WASP-121	2016-12-12	GROND	238	SDSS-r'	40/50/60	1.242	0.870	13.36	1.73 → 1.01 → 1.04
WASP-121	2016-12-12	GROND	238	SDSS-z'	40/50/60	1.244	1.759	13.39	1.73 → 1.01 → 1.04

Notes.
[a] Eliminated because its β-factor is larger than 2.5.
[b] Eliminated because its depth is more than 5σ away from the average.
[c] Eliminated because it is an outlier on the TTV-diagram for both linear and quadratic models.

3.1.6. Danish 1.54 m Observations

Three transits of WASP-19 b and one of WASP-103 b were obtained using the 1.54 m Danish Telescope at ESO La Silla, Chile, as a side-project of the MiNDSTEp microlensing observations (Dominik et al. 2010). We used the Danish Faint Object Spectrograph and Camera (DFOSC), which has a 13′.7 × 13′.7 field of view sampled at 0″.39 px^{-1}. A Bessell *R* or *I* filter was used for each transit. The observations were obtained with the telescope defocussed.

3.1.7. GROND Observations

We observed a transit of WASP-121 using the GROND (Gamma-Ray Burst Optical/Near-Infrared Detector; Greiner et al. 2008) imager on the MPG 2.2 m telescope at the ESO Observatory in La Silla (Chile). GROND obtains images simultaneously in four optical (SDSS g', r', i', z') and three infrared (J, H, K) bands, and has been used to observe many planetary transits previously (e.g., Mancini et al. 2014a, 2014b, 2016a, 2016b; Southworth et al. 2015, 2017) including the characterization of starspots (Mohler-Fischer et al. 2013; Mancini et al. 2013a; Biagiotti et al. 2024). Our main aim in the current work is to measure a precise transit time, so we used only the optical bands. These have a FoV of $5\overset{\prime}{.}2 \times 5\overset{\prime}{.}2$ sampled at $0\overset{\prime\prime}{.}16$ px^{-1} and were defocussed.

3.1.8. CAHA Observations

A transit of WASP-114 was observed with the Zeiss 1.23 m telescope at the Astronomical Observatory of Calar Alto in Spain, which has been extensively used for transit observations by our group (e.g. Ciceri et al. 2013; Mancini et al. 2017). The DLR-MKIII CCD camera gave a FoV of $21\overset{\prime}{.}5 \times 21\overset{\prime}{.}5$ at $0\overset{\prime\prime}{.}32$ px^{-1}. We used a Cousins R filter, defocussing and CCD windowing to maximize the quality of the data. The sky was clear but not photometric.

3.1.9. NTT Observations

Three transits of WASP-19 b were observed in February 2013 using the ESO New Technology Telescope (NTT), at La Silla, Chile, equipped with the ESO Faint Object Spectrograph and Camera (EFOSC2; Buzzoni et al. 1984). We heavily defocussed the telescope and observed in the R band (ESO filter #784), obtaining photometric precisions of approximately 0.5 mmag per point. Further details of this approach, and an example PSF can be found in Tregloan-Reed et al. (2013) and Tregloan-Reed & Southworth (2013). The third transit contains a clear spot-crossing event.

3.1.10. Loiano 1.52 m Observations

A complete transit event of TrES-1 b was recorded with the Cassini 1.52 m telescope from the Loiano Observatory (Italy), which at that time was part of the Astronomical Observatory of Bologna. The BFOSC (Bologna Faint Object Spectrograph and Camera) instrument was used to give images with a FoV of $13\overset{\prime}{.}0 \times 12\overset{\prime}{.}6'$ at $0\overset{\prime\prime}{.}58$ px^{-1}. The CCD was windowed, a Gunn-i filter was used, and the telescope was defocussed.

3.2. Data Reduction

3.2.1. AstroImageJ

All the observations performed with the T80, T100, IST60 and ATA050 telescopes were reduced using the AstroImageJ (hereafter AIJ; Collins et al. 2017b) software package, where standard calibration procedures (bias, dark, and flat corrections) were applied with the corresponding calibration frames obtained during the same nights. The observation times were converted to barycentric Julian Dates (hereafter BJD$_{\rm TDB}$) before performing ensemble photometry (Honeycutt 1992) with AIJ, using a set of comparison stars selected according to their brightness, color, and photometric stability in the observed passband. The aperture centers were manually determined to avoid misidentifications caused by centroid algorithms, especially in cases where defocused images produced complex PSFs. Finally, corrections for airmass and sky/pixel ratio were applied, and the relative fluxes derived with AIJ were normalized by fitting a line to the out-of-transit data points.

3.2.2. TESS

The Transiting Exoplanet Survey Satellite (TESS) observed all objects in our sample except WASP-103; see Table A1. For each sector we downloaded the 2 minutes cadence mode products of the Science Processing Operations Center (SPOC) pipeline (Jenkins et al. 2016) from the Barbara A. Mikulski Archive for Space Telescope (MAST) of the Space Telescope Science Institute (STScI) of NASA.[25] From the SPOC pipeline, we obtained the data validation timeseries (DVT) light curve products utilizing the LIGHTKURVE package (Lightkurve Collaboration et al. 2018) since instrumental artifacts and stellar variabilities were corrected in the LC_DETREND column of the relevant DVT-files. To improve accuracy and precision, we discarded apparent outliers linked to instrumental effects and split the full data set into smaller parts focused on single transit events using the ephemeris information provided in the corresponding DVT-files.

3.2.3. DEFOT

The data from the Danish telescope, the NTT, GROND, CAHA and Loiano were reduced using the DEFOT pipeline (Southworth et al. 2009a, 2014). This utilizes the IDL[26] implementation of the APER routine from DAOPHOT (Stetson 1987) contained in the NASA ASTROLIB library[27] to perform aperture photometry. We calculated master bias and flat-field images but did not use them as they increased the scatter in the data without changing the transit shapes.

A differential-magnitude light curve was generated for each transit observation by constructing a composite comparison star. This star was made by iteratively adjusting the weights of individual stars and the coefficients of a low-order polynomial to minimize the scatter in the data outside transit. The

---

[25] https://mast.stsci.edu/portal/Mashup/Clients/Mast/Portal.html

[26] https://www.ittvis.com/idl/

[27] http://idlastro.gsfc.nasa.gov/

timestamps for the midpoint of each image were taken from the headers of the FITS files and converted to $\mathrm{BJD_{TDB}}$ using routines from Eastman et al. (2010).

3.2.4. Exoplanet Transit Database and Literature work

Additional photometric data were obtained from the Exoplanet Transit Database[28] (hereafter ETD; Poddaný et al. 2010) and previous studies. For ETD light curves, we only included light curves with a data quality factor of 2 or lower (DQ $\leqslant$ 2) to avoid the influence of gaps or high noise levels, which can interfere with accurate mid-transit time measurements. Airmass values were first calculated for the observing site following the formulation given in Hiltner (1962), and all observation times provided in $\mathrm{JD_{UTC}}$ or $\mathrm{HJD_{UTC}}$ were converted to $\mathrm{BJD_{TDB}}$ using the relevant ASTROPY constants and functions (Astropy Collaboration et al. 2013, 2018). Airmass detrending and out-of-transit normalization were subsequently performed in AIJ. Literature data were processed in a similar manner: time stamps were converted to $\mathrm{BJD_{TDB}}$ when necessary, and light curves that were not already normalized or airmass-detrended underwent the same AIJ procedures to ensure a homogeneous data set.

3.3. Light Curve Selection Criteria

Before performing the construction of the TTV diagram, we excluded light curves that contained significant gaps within the transit or showed strong correlated noise, particularly during ingress and egress. The remaining light curves were modeled with EXOFAST (Eastman et al. 2013) (see Section 4.1 for details), after which we computed the photometric noise rate (PNR; Fulton et al. 2011) from the residuals as a measure of white noise. Light curves with PNR values exceeding the transit depth (i.e. PNR $> \delta$) were discarded. To assess red noise, we binned the residuals over intervals of ingress/egress duration ±5 minutes in 1 minute steps and calculated the β values following Winn et al. (2008). Light curves with a median β greater than 2.5 were rejected. Additionally, we excluded any light curves where the transit depth was a 5σ outlier for the corresponding planet. Finally, we omitted light curves that deviated from both the linear and quadratic fits to the TTV diagram by more than 5σ.

The only exception in our sample is KELT-9, for which the PNR–β analysis is not adequate. This system is strongly affected by gravity darkening due to the rapid stellar rotation ($v \sin i = 111.4 \pm 1.3$ km $\mathrm{s^{-1}}$; Gaudi et al. 2017), which makes the star oblate and produces a temperature gradient between the hotter poles and the cooler equator. As a result, transits across different stellar latitudes yield asymmetric light-curve shapes that cannot be well described by standard models, leading to strongly correlated residuals (Ahlers et al. 2020; Harre et al. 2023). In addition, stellar pulsations with a characteristic period of about 7.59 hr have been reported in KELT-9 (Wong et al. 2020), introducing quasi-periodic variability on time scales comparable to the transit duration ($T_{14} \approx 4$ hr; Gaudi et al. 2017). These two effects together generate excessive levels of time-correlated (red) noise, which results in artificially high β values and the rejection of the majority of light curves if the same criteria were applied. For this reason, KELT-9 data were treated as a special case, and its light curves were included in the analysis without the PNR–β filtering.

4. Analysis and Results

4.1. Light-curve Modeling and Measurements of Mid-transit Times

We adopted the procedure described in Baştürk et al. (2022) for modeling the light curves (Figure 2) and determining the mid-transit times and their uncertainties. In summary, the light curves were modeled with EXOFAST (Eastman et al. 2013), after converting the observation times into $\mathrm{BJD_{TDB}}$ and detrending them for airmass effects using AIJ when necessary. Throughout the study, we used the web version of the code (EXOFAST-V1).[29] The values of the stellar atmospheric parameters were taken from the NASA Exoplanet Archive and set as Gaussian priors, while the orbital periods of the planets were fixed. The limb-darkening coefficients were assigned uniform priors, retrieved from Claret & Bloemen (2011) based on the stellar parameters and the observational passbands. For passbands not directly available, the closest match in transmission curve was adopted (e.g., the I band for the TESS passband and *CoRoT* for Clear-filter observations). Since EXOFAST does not account for spot-induced asymmetries in transit light curves, spot-crossing features were neither explicitly modeled nor masked, and the light curves were fitted assuming a symmetric transit profile (Plavchan et al. 2020). The mid-transit time, initially treated as a free parameter, was derived from the contact points of the light curve model (Table 3). The program outputs this value along with its associated uncertainty and other fitted parameters—such as the total and full transit durations and the transit depth—which were subsequently used to verify the internal consistency of the results and their agreement with the known system parameters.

4.2. Transit Timing Variations (TTV) Analysis

After selecting the light curves based on the selection criteria described in Section 2, we constructed our TTV diagrams for each system in the sample according to the reference ephemeris information given in Table A8. For each target, we took into account all transit times from this study,

---

[28] https://var.astro.cz/en/Home/ETD

[29] https://exoplanetarchive.ipac.caltech.edu/cgi-bin/ExoFAST/nph-exofast

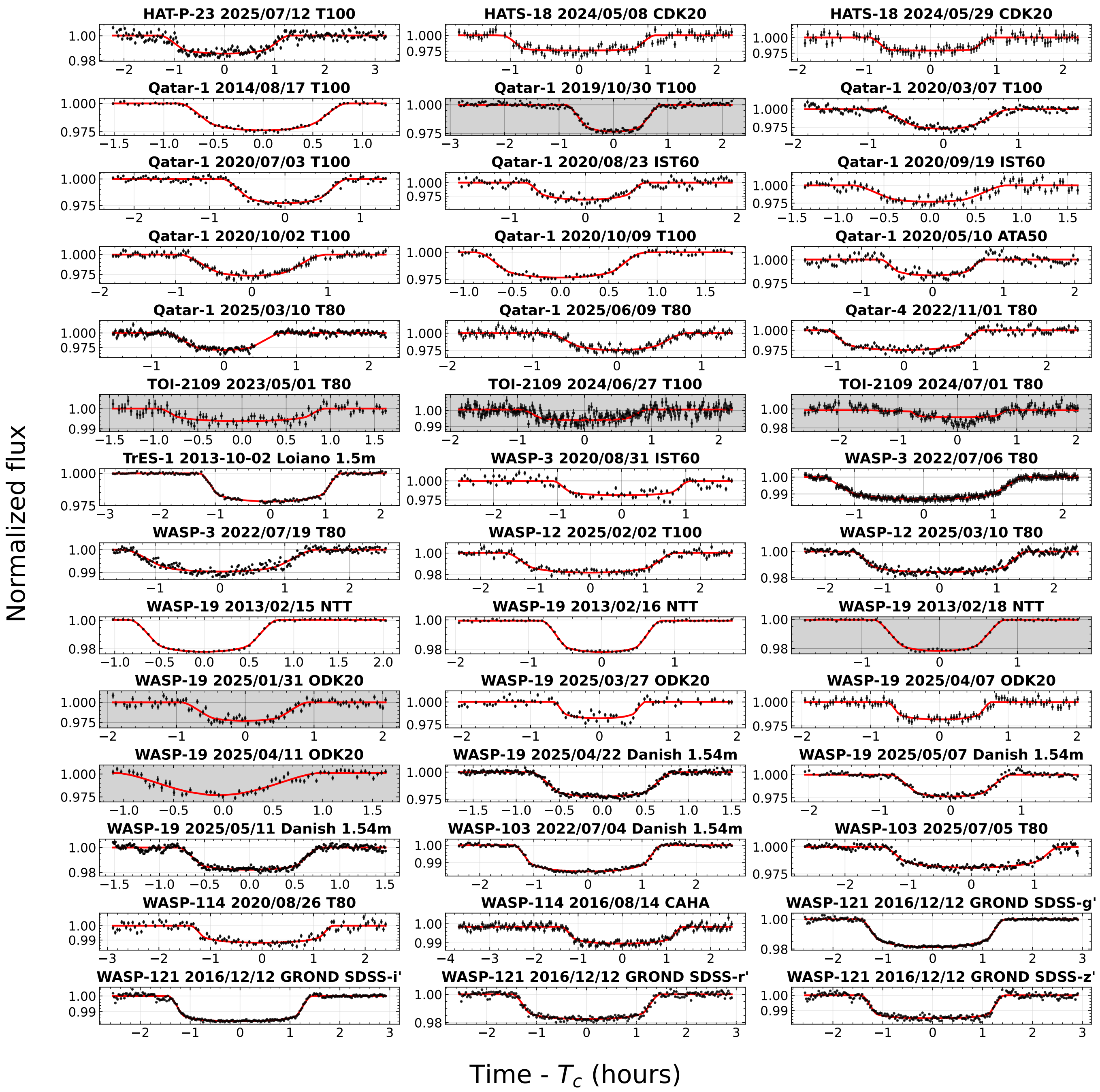

Figure 2. Light curves of the objects in our sample, as listed in Table 2. Individual exposures are shown in black, while the EXOFAST models are plotted in red. Light curves excluded from the sample due to PNR, β or 3σ clipping criterion are displayed with a gray background.

along with those reported in the literature that satisfied the following conditions: (*i*) the time system was explicitly specified as $\mathrm{BJD_{TDB}}$, (*ii*) the light curve consists of both the ingress and egress of the transit and (*iii*) we were not able to access its light curve to model ourselves. In the end, we obtained a total of 2930 minimum times for the whole sample, as listed in Table A3.

We fitted two models to the TTV diagram. The first model assumes a constant orbital period over time

$$T(E) = T_0 + P_{\mathrm{orb}} \times E. \tag{8}$$

Here, T_0 is the reference time of minimum, which is also given in Table A8.

On the other hand, the second model assumes a secular variation in the orbital period, allowing it to change linearly

Table 3
Measured Mid-transit Times and their Uncertainties

System	T_0 (BJD$_{\rm TDB}$)	σ (days)
HAT-P-23	2460869.39168	0.00070
HATS-18	2460439.60668	0.00082
HATS-18	2460460.55349	0.00086
Qatar-1	2456887.31479	0.00019
Qatar-1	2456234.10349	0.00023
…	…	…

Note. The order of measured mid-transit times is as the same as Table 2.

with time. In this case, the ephemeris can be expressed as

$$T(E) = T_0 + P_{\rm orb} \times E + \frac{1}{2}\frac{dP_{\rm orb}}{dE} \times E^2, \tag{9}$$

where $dP_{\rm orb}/dE$ represents the time derivative of the orbital period. In the case of exoplanetary systems, the measured period variations are typically on the order of a few nano-days per orbital cycle (e.g., WASP-12 b, $dP_{\rm orb}/dE = -5.364 \times 10^{-10}$ d cycle^{-1}; Kutluay et al. 2023). So, to help the reader along the way, it is more beneficial to read the results in a more meaningful scale. A positive value of the quadratic term indicates that the orbital period is increasing over time, whereas a negative value implies a decreasing period.

In both cases, we have drawn samples from Gaussian priors for the model parameters, with the priors centered on values obtained from an initial non-linear least-squares fit and widths set according to the corresponding uncertainties. Sampling from these prior distributions was performed using 16 Markov chains of 5000 iterations, 500 of which are discarded as burn-in. For each sample, the log-likelihood was computed, allowing the construction of posterior distributions for the model parameters. The posterior samples were subsequently obtained after discarding an initial burn-in period. The probabilistic fitting was conducted using the current (fifth) version of PYMC5[30] (Abril-Pla et al. 2023), while the preliminary nonlinear least-squares fits were performed with LMFIT (Newville et al. 2016) to obtain reliable initial values for the fit parameters.

To assess which model provides a better representation of the timing data, we employed the reduced chi-square statistic (χ^2_ν), the Bayesian Information Criterion (BIC; Schwarz (1978); Liddle (2007)) and the Akaike Information Criterion (AIC; Akaike (1974)). To further quantify the relative performance between the linear and quadratic models, we computed the difference in their Information Criterion values, defined as

$$\Delta{\rm BIC} = {\rm BIC}_{\rm quadratic} - {\rm BIC}_{\rm linear}, \tag{10}$$

and

$$\Delta{\rm AIC} = {\rm AIC}_{\rm quadratic} - {\rm AIC}_{\rm linear}. \tag{11}$$

Following the conventional interpretation (Raftery 1995), a difference of $|\Delta{\rm BIC}| > 10$ is considered strong evidence in favor of the model with the lower BIC value and likewise for $|\Delta{\rm AIC}|$. For systems with $|\Delta{\rm BIC}| < 10$, the improvement of the leading model is not statistically significant. In such cases, we only updated the linear ephemeris using Equation (8). Figures 3, 4, 5 and 6 present the TTV diagrams of the systems with updated ephemerides and we present the results of the TTV analysis in Table 4. We investigated whether periodic or quasi-periodic variations are present in the TTV data based on Lomb–Scargle (hereafter LS) periodograms (Lomb 1976; Scargle 1982) by employing the relevant function in the ASTROPY package (VanderPlas 2018). We only considered the cases where we observed peaks with a False Alarm Probability (FAP) value smaller than 0.1% and investigated the potential reasons of the signal.

4.3. Modeling the Efficiency of Tidal Dissipation Using MESA

To complement the TTV analysis, we have also constructed models of each of the host stars in our sample based on the parameters reported in Table 1 using MESA version r24.08.1 (Paxton et al. 2011, 2013, 2015, 2018, 2019; Jermyn et al. 2023), along with stellar parameters from MIST (Choi et al. 2016; Dotter 2016). In each case, we adopted an initial metallicity of 0.02 (unless otherwise specified) and the shortest reported rotation period constraint in the literature (purely for computation of the tidal period—the stellar models themselves omit rotation). We integrated these models until the end of the main sequence or to the maximum reported age in Table 1, whichever is shorter, with a few exceptions that integrated for longer. This allowed us to obtain radial profiles (r is the spherical radius from the stellar center) for the stellar density $\rho(r)$, pressure $p(r)$, gravitational acceleration $g(r)$, and other variables, as a function of stellar age. Using these profiles, we calculated the tidal response following the approach described in Barker (2020). We first computed the equilibrium tide response, and hence the viscous dissipation of this component (see Equation 23 in Barker (2020)). We then computed the wavelike response and the resulting dissipation using Equations (3) and (4).

4.4. Individual Results

4.4.1. CoRoT-2

CoRoT-2 b (CoRoT-Exo-2 b) is the second transiting planet discovered by the *Convection, Rotation and planetary Transits* (CoRoT) mission (Alonso et al. 2008). Several studies have investigated possible orbital period changes driven by tides.

---

[30] https://www.pymc.io/welcome.html

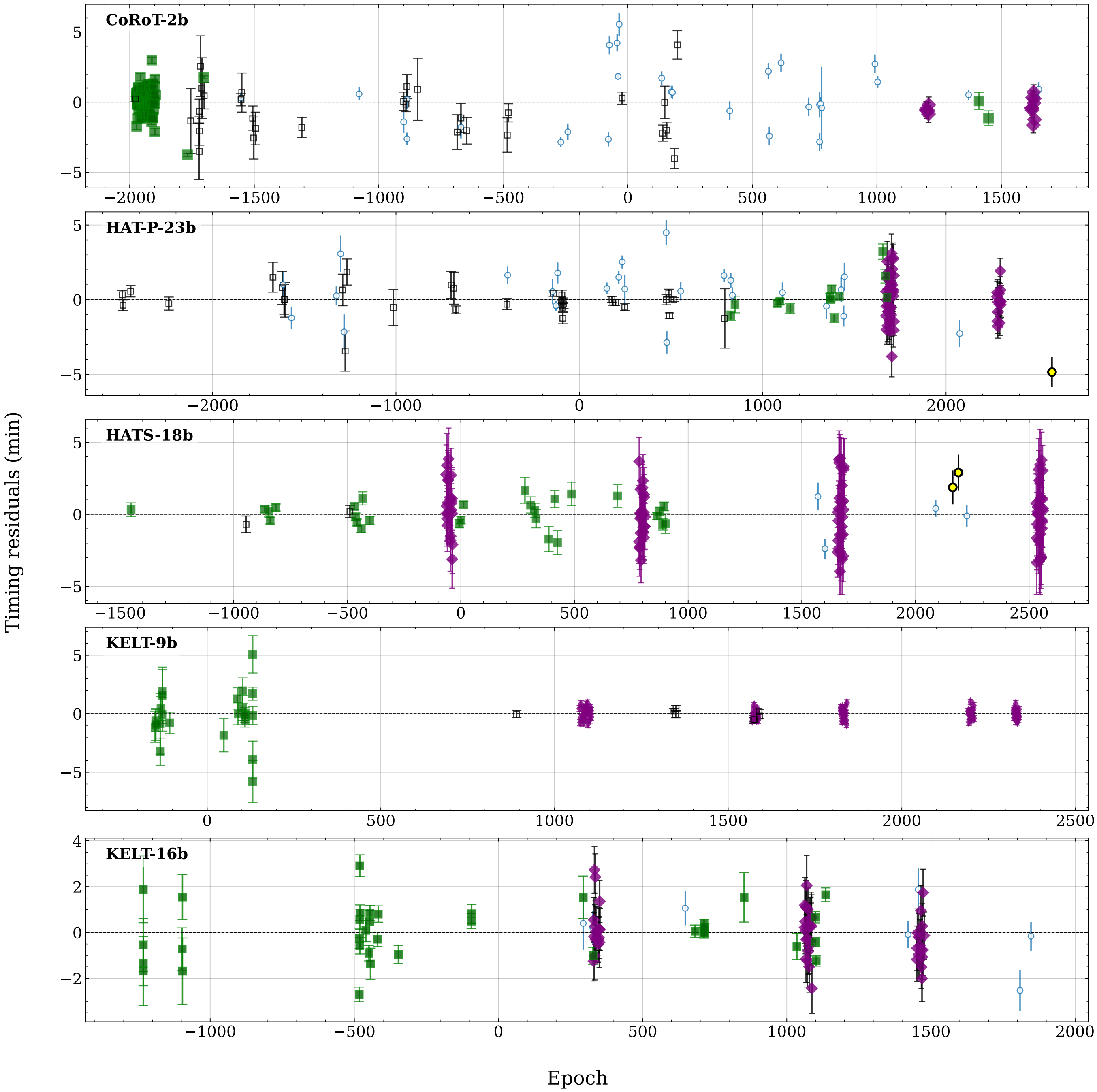

Figure 3. Linear residuals of the TTV diagrams for CoRoT-2 b, HAT-P-23 b, HATS-18 b, KELT-9 b and KELT-16 b based on observations from various sources: ETD data (blue empty circles), obtained and analyzed literature light curves (green squares), adopted literature transit times (empty black squares), this work (black and yellow circles) and TESS observations (purple circles).

While early and recent analyses have yielded conflicting results, some finding no significant decay and others reporting evidence in favor of orbital decay, the system remains an important and debated target for tidal evolution studies (Öztürk & Erdem 2019; Ivshina & Winn 2022; Adams et al. 2024; Wang et al. 2024). Before the TTV analysis results, it should be noted that the light curve data originally provided by Öztürk & Erdem (2019) were obtained from the corrected versions of Adams et al. (2024), who pointed out that the time stamps in Öztürk & Erdem (2019) were given in JD rather than HJD or BJD.

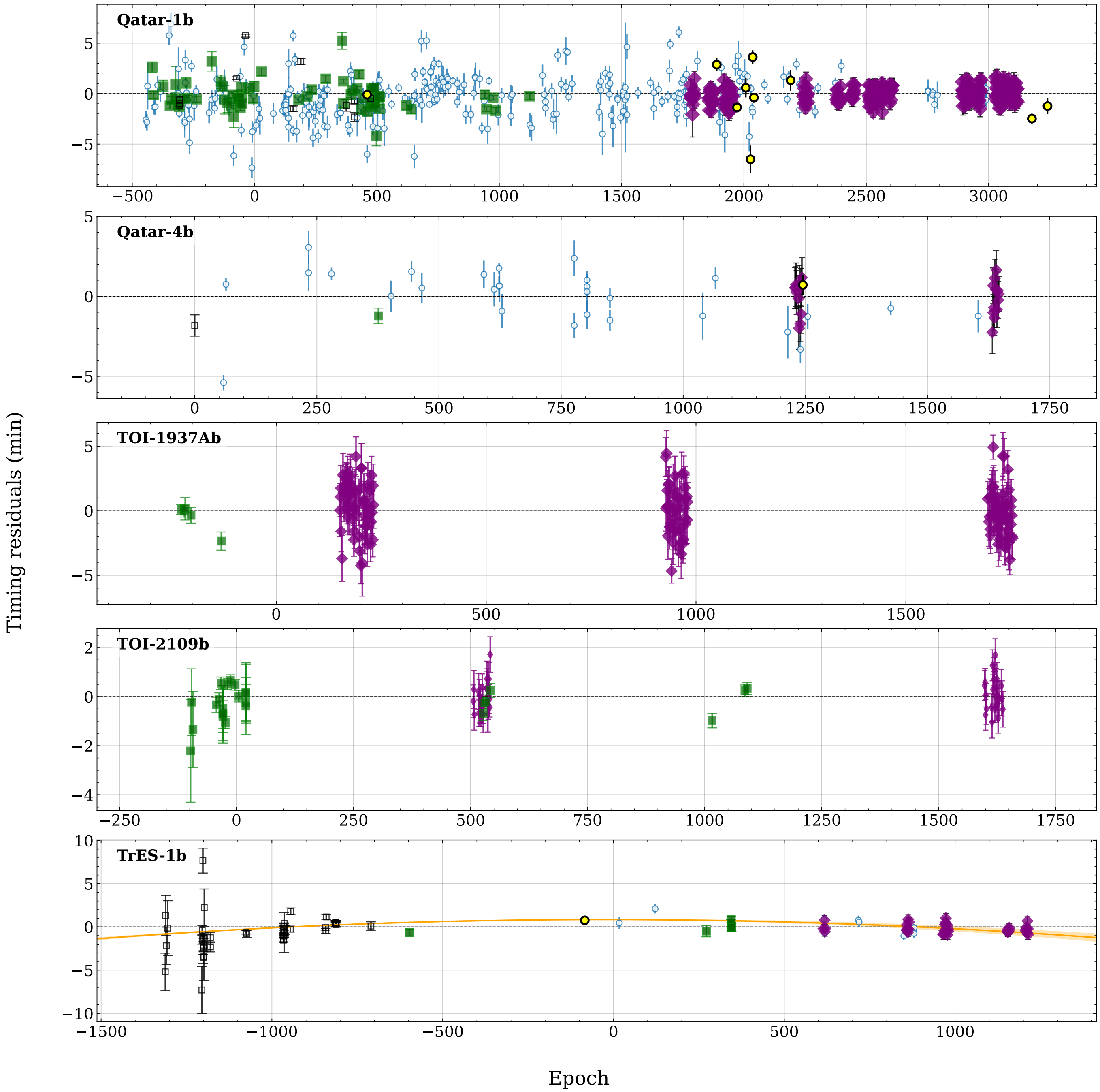

Figure 4. Same as Figure 3, but for Qatar-1 b, Qatar-4 b, TOI-1937A b, TOI-2109 b and TrES-1 b. Since $|\Delta\mathrm{BIC}| > 10$ for TrES-1 b case, we also present the median orbital decay model represented with the orange line and the shaded band indicating its 3σ uncertainty range.

The obtained values of $\Delta\mathrm{AIC} = 1.93$ and $\Delta\mathrm{BIC} = 4.97$ indicate only a mild preference for the linear model, but this preference is inconclusive. The quadratic model yields a positive period change of $3.4 \pm 1.9\,\mathrm{ms\,yr^{-1}}$, which is unexpected from tidal theory, since for $P_{\mathrm{orb}} < P_{\mathrm{rot}}$ we predict angular momentum transfer from the orbit to the stellar rotation. We therefore constrain the stellar tidal quality factor $Q'_{\star}$ using the 3σ lower limit of the quadratic coefficient, $a_1^{lim} = 0.5 \times dP/dE = -1.68 \times 10^{-11}$ d cycle^{-1}, following Southworth et al. (2022). This corresponds to a 99.7% confidence limit of $Q'_{\star} > (5.27 \pm 0.87) \times 10^5$.

The strongest peak in the LS periodogram of the TTV diagram for CoRoT-2 b is observed at 470.0 d with a FAP value of 3.2×10^{-5}. However, when we phase the TTV diagram with this

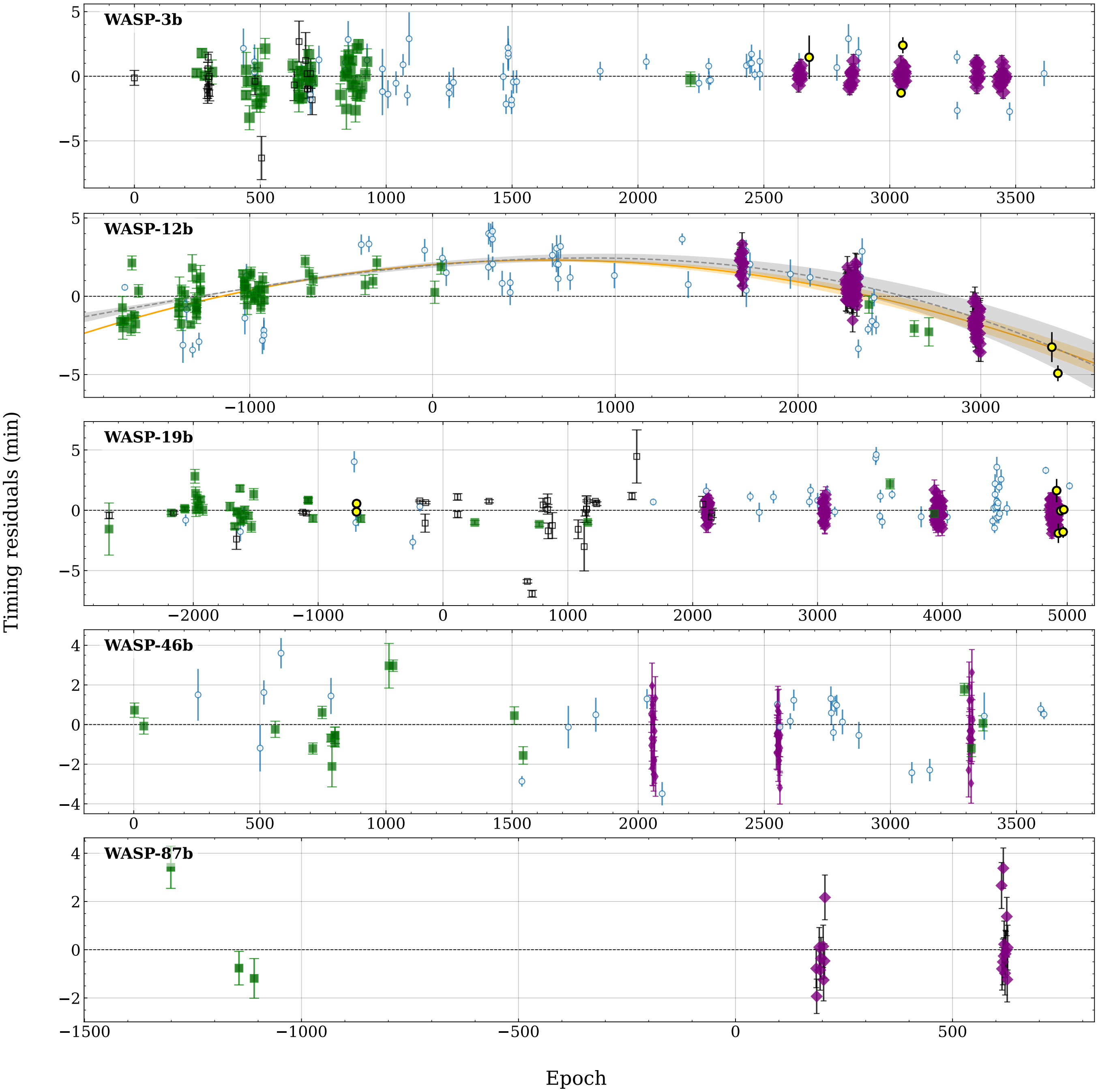

Figure 5. Same as Figure 3, but for WASP-3 b, WASP-12 b, WASP-19 b, WASP-46 b and WASP-87 b. Since $|\Delta\mathrm{BIC}| \gg 10$ for WASP-12 b case, we present the median orbital decay model represented with the orange line and the shaded band indicating its 3σ uncertainty range. Additionally, we show the median of the decay acceleration model in black dashed lines and its 3σ uncertainty range in a gray band.

periodicity and the integer divisors of it, we do not observe any agreement with the periodic models. Although there is a nearby, potentially bound source (Gaia DR3 4287820852697823872) in Gaia data, this G = $15^{\mathrm{m}}.46$-star is unlikely to be the source of the signal because it is separated from CoRoT-2 by $4\overset{''}{.}08 \pm 0\overset{''}{.}03$ arcsec at ∼210 pc, which corresponds to a linear distance more than 850 au. There have also been no mentions of any other outside perturber in the literature.

Theoretical models of CoRoT-2 following the approach outlined in Section 4.3 provide us with $Q'_{\mathrm{IGW}} = 1.94 \times 10^{6}$ at an age of 2.7 Gyr (the value is not strongly sensitive to age), assuming fully damped gravity waves. The star is of solar type

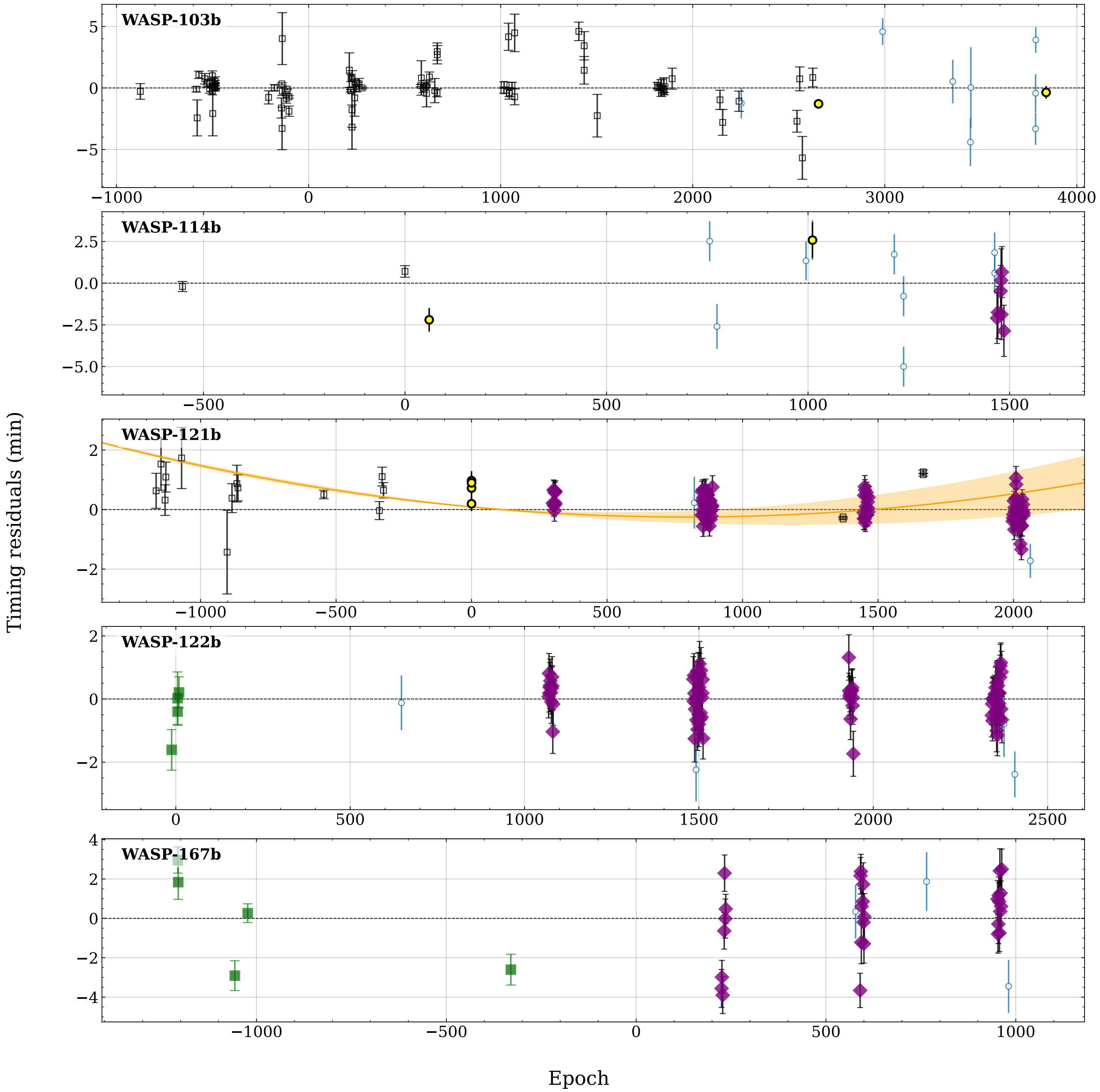

Figure 6. Same as Figure 3, but for WASP-103 b, WASP-114 b, WASP-121 b, WASP-122 b and WASP-167 b. Since $|\Delta\mathrm{BIC}| > 10$ for the WASP-121 b case, we also present the median quadratic model represented with the orange line and the shaded band indicating its 3σ uncertainty range.

with a radiative core, and the critical planetary mass required for wave breaking is $M_{\rm crit}/M_{\rm J} = 1.4$ at the same age. Hence, the planet is predicted to be sufficiently massive to induce wave breaking in the stellar core, and we predict the planet to be spiraling into the star, but at a slower rate (larger $Q'_\star$) than the lower bound observational constraint. Equilibrium tides are predicted to be negligibly weak, and inertial waves cannot be excited in the convective envelope (for an aligned orbit) as the tidal period exceeds $P_{\rm rot}/2$.

4.4.2. HAT-P-23

HAT-P-23 b is a HJ with a mass of 1.97 $M_{\rm J}$ and an inflated radius of 1.37 $R_{\rm J}$, orbiting a G0-type star of $\sim$1.1 $M_\odot$ with

Table 4

Median-fit Results from Our TTV Analysis, Presented for Both the Linear Model Representing the Constant Period and the Quadratic Model that Accounts for Orbital Decay

					Quadratic Model		
System	ΔAIC	ΔBIC	$P_{\rm orb}$[c] (days)	T_0[b,c] ($\rm BJD_{TDB}$)	$a_{\rm quad}$[d] (d $\rm cycle^{-1}$)	$dP_{\rm orb}/dt$ (ms $\rm yr^{-1}$)	$Q'_\star$[a]
CoRoT-2	1.93	4.97	1.7429971349(2)	57683.441534(37)	$3.14^{+1.61}_{-1.69} \times 10^{-11}$	1.14 ± 0.58	$>5.27 \pm 0.87 \times 10^5$
HAT-P-23	1.77	4.60	1.2128864160(2)	57742.573862(29)	$1.53^{+1.33}_{-1.32} \times 10^{-11}$	0.80 ± 0.69	$>1.41 \pm 0.45 \times 10^5$
HATS-18	1.72	4.65	0.8378438220(45)	58626.511345(37)	$3.06^{+3.29}_{-3.31} \times 10^{-11}$	2.31 ± 2.48	$>6.74 \pm 2.04 \times 10^5$
KELT-9	1.97	4.75	1.4811189635(34)	57095.685686(62)	$1.06^{+2.25}_{-2.60} \times 10^{-11}$	0.45 ± 0.96	$>1.21 \pm 0.37 \times 10^6$
KELT-16	−0.68	1.88	0.9689926792(51)	58392.597911(42)	$-2.57^{+0.68}_{-0.68} \times 10^{-10}$	-16.76 ± 4.48	$>1.03 \pm 0.21 \times 10^6$
Qatar-1	3.00	6.54	1.4200242456(12)	56234.103712(21)	$<10^{-13}$	< 0.006	$>1.16 \pm 0.09 \times 10^5$
Qatar-4	−4.80	−2.74	1.8053646151(39)	57637.774877(13)	$-1.68^{+0.21}_{-0.20} \times 10^{-9}$	-59 ± 7	$>1.10 \pm 0.40 \times 10^4$
TOI-1937A	1.98	5.05	0.9466794627(95)	59085.910210(96)	$-0.73^{+1.71}_{-1.67} \times 10^{-10}$	-5 ± 11	$<3.4 \pm 0.1 \times 10^9$
TOI-2109	−1.16	1.09	0.6724740164(57)	59378.459298(46)	$2.77^{+1.13}_{-1.12} \times 10^{-10}$	26 ± 11	$>1.23 \pm 0.20 \times 10^6$
TrES-1	−13.57	−11.02	3.0300696522(27)	56822.891950(88)	$-7.14^{+2.86}_{-2.86} \times 10^{-11}$	-14.9 ± 0.6	$5.7 \pm 0.6 \times 10^2$
WASP-3	1.32	4.64	1.8468351793(20)	54143.851121(47)	$-4.82^{+1.89}_{-2.26} \times 10^{-11}$	-1.6 ± 0.8	$>3.8 \pm 1.3 \times 10^6$
WASP-12	−189.70	−186.25	1.0914193645(14)	57010.513047(20)	$-5.08^{+0.01}_{-0.01} \times 10^{-10}$	-29.4 ± 4.0	$1.72 \pm 0.18 \times 10^5$
WASP-19	1.96	5.63	0.7888390012(58)	56885.482609(15)	$-2.27^{+2.36}_{-2.44} \times 10^{-12}$	-0.18 ± 0.19	$>5.0 \pm 0.7 \times 10^6$
WASP-46	−1.13	1.36	1.4303721864(35)	55392.316213(75)	$2.36^{+0.24}_{-0.22} \times 10^{-10}$	10.4 ± 1.1	⋯
WASP-87	−1.51	−0.33	1.6827943515(95)	58276.860909(122)	$1.20^{+0.21}_{-0.21} \times 10^{-9}$	47 ± 8	⋯
WASP-103	0.68	3.12	0.9255454474(24)	57308.324556(16)	$-5.30^{+2.03}_{-2.01} \times 10^{-11}$	-2.0 ± 0.7	$>1.83 \pm 0.17 \times 10^6$
WASP-114	−0.56	0.94	1.5487751950(12)	57522.659955(123)	$-5.10^{+1.53}_{-1.53} \times 10^{-10}$	-35 ± 10	$>4.7 \pm 0.6 \times 10^5$
WASP-121	−16.82	−13.84	1.2749244026(31)	58119.720671(16)	$3.70^{+0.21}_{-0.22} \times 10^{-10}$	15.1 ± 0.8	⋯
WASP-122	−1.13	1.32	1.7100531597(69)	56665.225124(123)	$-1.65^{+0.59}_{-0.63} \times 10^{-10}$	-19 ± 7	$>4.6 \pm 0.5 \times 10^4$
WASP-167	−3.81	−5.4	2.0219566280(13)	58117.023535(109)	$3.8^{+1.3}_{-1.3} \times 10^{-10}$	11.8 ± 4.1	$>10.9 \pm 0.11 \times 10^7$

Notes. In cases where dP/dE (or equivalently dP/dt) is positive—indicating orbital growth—the 3σ lower limit is adopted to derive a lower bound on reduced tidal quality factor $Q'_\star$ of the host star at 99.7% confidence level. It should be noted that the uncertainties on $Q'_\star$ come from the uncertainties on other parameters given in Equation (2).

[a] The 3σ lower limit on $Q'_\star$ is calculated from the lower limit of $\dot{P}$ (or dP/dE); no value is provided if $\dot{P} - 3\sigma$ is positive.

[b] $\rm BJD_{TDB}$ - 2,400,000.

[c] We provide T_0 and $P_{\rm orb}$ according to the quadratic ephemerides for TrES-1 b, WASP-12 b and WASP-121 b since their quadratic ephemeris represents the timing data better.

[d] $a_{\rm quad} = \frac{1}{2}\frac{dP}{dE}$.

$P_{\rm orb} = 1.21$ days (Bakos et al. 2011; Ciceri et al. 2015; Bonomo et al. 2017). The orbit is approximately aligned with the stellar spin axis ($\lambda = 15^\circ \pm 22^\circ$; Moutou et al. (2011)). Several studies have searched for evidence of orbital decay and constrained the stellar tidal quality factor $Q'_\star$, consistently finding only lower limits and no significant evidence for ongoing decay. The most recent analysis likewise concludes that orbital decay has not yet been detected in the HAT-P-23 system (Maciejewski et al. 2018b; Patra et al. 2020; Maciejewski et al. 2022; Alvarado et al. 2024).

As in previous works, our analysis reveals no significant evidence of orbital decay for this planet. We found ΔAIC = 1.77 and ΔBIC = 4.60, favoring the constant period model over the changing orbital period model. The median quadratic fit suggests a period change of 0.80 ± 0.69 ms $\rm yr^{-1}$. Considering the spin-orbit relationship, this outward migration would not be predicted theoretically. Still, we calculated a lower limit of the stellar tidal quality factor $Q'_\star >$ $(1.41 \pm 0.45) \times 10^5$ using the 99.7% level confidence level, with $a_1^{lim} = -4.19 \times 10^{-11}$ day $\rm cycle^{-1}$.

Theoretical models of HAT-P-23 indicate that fully damped gravity waves would provide $Q'_{\rm IGW} = 6.7 \times 10^5$ at 4 Gyr. The star possesses a convective core, and wave breaking of these waves near the center is not predicted, which makes it difficult to justify the fully damped regime being relevant (unless magnetic wave conversion is in operation, which is not predicted according to Duguid et al. 2024). Hence, we would not clearly predict orbital decay, though if the gravity waves are fully damped, they would provide such a value of $Q'_{\rm IGW}$. The star likely rotates sufficiently slowly ($P_{\rm rot} = 7.015$ days; Salisbury et al. (2021)) to preclude inertial wave excitation.

4.4.3. HATS-18

HATS-18 b ($M_{\rm p} = 1.98\,M_{\rm J}$, $R_{\rm p} = 1.34\,R_{\rm J}$), orbiting a G V type solar-like star with $P_{\rm orb} \approx 0.83$ day, was discovered by

Penev et al. (2016). The nearly solar-mass ($1.04\,M_\odot$) and solar-age (4.2 ± 2.2 Gyr) host star would be expected to rotate with a period of ∼30 days (Barnes et al. 2016), yet observations indicate a much faster rotation of ∼9 days, possibly due to tidal spin-up by the close-in giant planet. Several studies have investigated orbital decay; no detectable period change has been found and the stellar tidal quality factor is constrained to $Q'_\star > 1.3 \times 10^5$ (Southworth et al. 2022) and refined to $Q'_\star > 3.5 \times 10^5$ with recent TESS observations (Maciejewski et al. 2024).

Overall, our analysis yields $\Delta\mathrm{AIC} = 1.72$ and $\Delta\mathrm{BIC} = 4.65$, suggesting that there is no evidence to favor orbital decay within the system. Hence, similar to the cases of CoRoT-2 b and HAT-P-23 b, we constrained the stellar tidal quality factor $Q'_\star$ using the 3σ lower limit $a_1^{lim} = -1.364 \times 10^{-10}$ day cycle^{-1}. This provides the constraint $Q'_\star > 6.8 \pm 2.0 \times 10^5$, which is in agreement with the findings of Southworth et al. (2022) and Maciejewski et al. (2024).

Based on the models presented in Southworth et al. (2022), we predict $Q'_{\mathrm{IGW}} \approx 1.2 \times 10^5$ for gravity waves in the fully damped regime. This regime is likely to be appropriate because the planet's mass exceeds the critical mass required for wave breaking at its current age. Hence, we would predict this planet to be undergoing orbital tidally-driven orbital decay. This is an exciting system for future studies, as we predict orbital decay with a value of Q'_{IGW} that is quite similar to the current observational constraint for its lower bound. Hence, future observations of this system would be worthwhile to constrain tidal theory.

4.4.4. KELT-9

This system lies at the extreme end of the sample, particularly in terms of stellar temperature. KELT-9 b, the hottest known exoplanet with $T_{\mathrm{eq}} = 4050$ K, is a $2.88\,M_{\mathrm{J}}$ inflated HJ ($1.9\,R_{\mathrm{J}}$) orbiting a B9.5–A0 type star of $1.98\,M_\odot$ and $T_{\mathrm{eff}} \sim 10{,}000$ K with $P_{\mathrm{orb}} \approx 1.5$ days (Gaudi et al. 2017; Hoeijmakers et al. 2019). The host is a fast rotator ($v \sin i = 111.4 \pm 1.3$ km s^{-1} or $P_{\mathrm{rot}} = 18.96 \pm 0.34$ hr; Jones et al. (2022)), with $P_{\mathrm{orb}} > P_{\mathrm{rot}}$, implying tidal angular momentum transfer from the star to the orbit and possible orbital expansion. Harre et al. (2023) found no evidence for a secular orbital period change and attributed the TTV signal to apsidal precession, despite the orbit being reported as circular by Gaudi et al. (2017). This scenario is supported by RV data from Stephan et al. (2022) and is discussed further in Section 5.1.

Our analysis resulted in $\Delta\mathrm{AIC} = 1.97$ and $\Delta\mathrm{BIC} = 4.75$, indicating that there is no statistically significant evidence for orbital decay or expansion. The orbital decay model suggests a change of 0.45 ± 0.96 ms yr^{-1}. To constrain $Q'_\star$, we took the 3σ lower limit $a_1^{lim} = -6.751 \times 10^{-11}$ day cycle^{-1}. However, since the HJ has a retrograde and polar orbit, we took the tidal factor[31] as $-135/16$ rather than $-27/2$ (see Table 2 in Harre et al. (2023)) while utilizing Equation (2). Thus, we provide a lower bound to $Q'_\star > (1.21 \pm 0.37) \times 10^6$.

Our theoretical models of KELT-9 provide $Q'_{\mathrm{IGW}} > 10^{12}$ for the $l = m = 2$ tide at 0.3 Gyr based on waves excited from the interface with the convective envelope, and hence negligible tidal migration. On the other hand, the star rotates rapidly enough for inertial waves to be excited in the envelope, leading to $Q'_{\mathrm{IW}} \sim 10^{10}$ for a similar age. Equilibrium tides are also predicted to be weak with $Q'_{\mathrm{eq}} \sim 3 \times 10^{12}$. Gravity waves launched from the convective core may be more important in this star but they are unlikely to provide sufficient dissipation to predict observable orbital expansion. On the other hand, the polar orbit suggests other tidal components could be excited than the ones we consider here.

4.4.5. KELT-16

KELT-16 b ($M_{\mathrm{p}} = 2.75\,M_{\mathrm{J}}$, $R_{\mathrm{p}} = 1.415\,R_{\mathrm{J}}$) is one of the few planets with $P_{\mathrm{orb}} < 1$ day and is therefore a promising target for detecting orbital period changes (Oberst et al. 2017). It orbits an F7V star ($1.21\,M_\odot$, $1.36\,R_\odot$) that has a distant M-dwarf companion at ∼300 au, which may have driven the planet inward via Kozai–Lidov oscillations (Oberst et al. 2017). With $T_{\mathrm{eq}} = 2453$ K, KELT-16 b is classified as an ultra-hot Jupiter. Using tidal evolution models, Oberst et al. (2017) showed that the planet could be tidally disrupted for $Q'_\star \sim 10^5$. Several studies have searched for evidence of orbital decay. While early analyses reported constraints on $Q'_\star$ and tentative period variations (Maciejewski et al. 2018b; Patra et al. 2020), subsequent investigations have found no statistically significant evidence for ongoing orbital decay to date (Maciejewski et al. 2022; L. Mancini et al. 2022; Harre et al. 2023; Alvarado et al. 2024).

From our analysis, we found $\Delta\mathrm{AIC} = -0.68$ and $\Delta\mathrm{BIC} = 1.88$. Hence, we still do not have convincing evidence from TTV supporting the shrinking orbit of KELT-16 b. Our quadratic fit suggests orbital decay, though with an orbital period change of -16.8 ± 4.5 ms yr^{-1}. Using the 95% confidence upper limit on the decay rate, we thus constrain the stellar tidal quality factor to $Q'_\star > (1.03 \pm 0.21) \times 10^6$.

Theoretical models of KELT-16 b predict $Q'_{\mathrm{IGW}} \approx 1.5 \times 10^6$ at 2 Gyr, albeit a slightly younger age than the one listed in Table 1 (Oberst et al. 2017). More efficient dissipation would be predicted for later ages. The star possesses a convective core and wave breaking of these waves is not predicted. Magnetic wave conversion (Duguid et al. 2024) remains a possibility to justify the fully damped gravity wave regime, but this is uncertain, depending on the age of the star. The star probably rotates too slowly for inertial waves to be excited. Our theoretical predictions

---

[31] The tidal factor f corresponds to the numerical coefficient $-27/2$ in Equation (2), which arises from the equilibrium tide formalism under the assumption of a prograde orbit.

are close to the current observational constraint, making this an exciting system for follow-up studies.

4.4.6. Qatar-1

Qatar-1 b ($M_\mathrm{p} = 1.29\,M_\mathrm{J}$, $R_\mathrm{p} = 1.14\,R_\mathrm{J}$; Collins et al. (2017a)) is the first planet discovered by the Qatar Exoplanet Transit Survey (Alsubai et al. 2011). This HJ orbits a K3V dwarf star ($T_\mathrm{eff} = 4861 \pm 25$ K) with $P_\mathrm{orb} = 1.42$ days. In-transit and out-of-transit radial velocity (RV) measurements indicate a circular orbit within 2σ and a well-aligned configuration ($\lambda = -8^\circ\!.4 \pm 7^\circ\!.1$); Covino et al. 2013. Early timing analyses suggested possible orbital period variations (von Essen et al. 2013), but subsequent studies using extended baselines found no evidence for a changing period (Maciejewski et al. 2015; Collins et al. 2017a; Mannaday et al. 2022).

We found that $\Delta\mathrm{AIC} = 3.00$ and $\Delta\mathrm{BIC} = 6.54$, hence no convincing evidence of orbital decay from our linear and quadratic models. Our median quadratic model yields a quadratic coefficient $a = (0.00425^{+1.33}_{-1.28}) \times 10^{-11}$ day cycle^{-1} which is consistent with zero ($|a|/\sigma_\mathrm{avg} \approx 0.003$). The corresponding rate of period change is $0.0^{+0.58}_{-0.55}$ s yr^{-1}. Using the 3σ lower limit on the quadratic coefficient $a_\mathrm{l}^\mathrm{lim} = -3.83 \times 10^{-11}$ day cycle^{-1}, we therefore constrain the stellar tidal quality factor as $Q'_\star > (1.16 \pm 0.09) \times 10^5$ in 99.7% confidence level.

Theoretical models of Qatar-1 predict that gravity waves in the fully damped regime would provide $Q'_\mathrm{IGW} \approx 1.85 \times 10^5$ at 11.6 Gyr. The planet exceeds the critical mass for wave breaking in this model ($0.5\,M_\mathrm{J}$), which makes the likely operation of wave breaking a good justification for the fully damped regime. We would thus predict the orbit to be decaying with $Q'_\mathrm{IGW} \approx 1.85 \times 10^5$. This is approximately at the same level as the lower bound observational constraint, making future observations particularly worthwhile.

We found two statistically significant peaks in the LS periodogram of the TTV diagram for Qatar-1 in the high-frequency regime at 3.8 and 12.9 days, and two more in the low-frequency regime (at 50.5 and 613.8 days). However, our Keplerian fits based on these periods do not perform better than the linear fit. Qatar-1 is also known to be an active star. Although von Essen et al. (2013) reported a tentative periodic TTV signal at ∼190 days, we have not detected any peaks on our LS periodogram at the corresponding frequency. Later studies on the TTVs observed in Qatar-1 found different periodicities, although they are not statistically significant (Maciejewski et al. 2015; Su et al. 2021; Mannaday et al. 2022). We believe that the frequencies that we and other studies have found through frequency analyses of the TTV data can be related to the activity of the star, which has been shown to be moderate in strength by Covino et al. (2013) based on the emission profiles of Ca II H&K lines in the HARPS data.

4.4.7. Qatar-4

Qatar-4 b ($M_\mathrm{p} = 6.10\,M_\mathrm{J}$ and $R_\mathrm{p} = 1.13\,R_\mathrm{J}$; Alsubai et al. 2017) is an HJ orbiting around an early K-type star ($V = 13.6$ mag and $T_\mathrm{eff} = 5215$ K; Alsubai et al. 2017) in $P_\mathrm{orb} = 1.8$ days. The host-star is comparatively young with an age of 0.17 Gyr (Alsubai et al. 2017). The system has been subject to discussion for timing analyses only a few times (Mallonn et al. 2019; Ivshina & Winn 2022) and no proof of a decaying orbit has been found yet.

Our analysis yielded $\Delta\mathrm{AIC} = -4.80$ and $\Delta\mathrm{BIC} = -2.74$. Hence, we conclude that there is no significant evidence for orbital decay with the current dataset. Our median orbital decay model suggests an orbital period change of -59 ± 7 ms yr^{-1}. Finally, we provide a constraint on the stellar tidal quality factor as $Q'_\star > 1.1 \pm 0.4 \times 10^4$.

Our models of Qatar-4 indicate $Q'_\mathrm{IGW} \approx 1.63 \times 10^6$ at 0.15 Gyr if the gravity waves are fully damped, and that wave breaking is not predicted in the stellar core. This means that the fully-damped regime may not be appropriate, so it is unclear whether the planet's orbit should be decaying at the rate that would be predicted using this value, or whether tidal dissipation would be less efficient due to partial radiative damping of gravity waves. The star rotates too slowly for inertial waves to be excited by the planet.

In the LS periodogram of Qatar-4, there are two strong peaks at 29.6 and 47.3 days with FAP values smaller than 10^{-5}. Qatar 4 displays out-of-transit variability due to its strong magnetic activity, as expected from its rather young age (Zak et al. 2025). Based on the variability in WASP data, Zak et al. (2025) found 7.07 ± 0.08 days for the rotation period. No non-zero eccentricity for its orbit, or evidence for an outside perturber, has been reported so far, making activity-induced pseudo-shifts in the transit centers the primary candidate for the reason of the peaks on the LS periodogram.

4.4.8. TOI-1937A

TOI-1937A b is an ultra-short-period planet with $M_\mathrm{p} = 2.01\,M_\mathrm{J}$ and $R_\mathrm{p} = 1.25\,R_\mathrm{J}$, orbiting a Sun-like star ($T_\mathrm{eff} = 5814$ K, $M_\star = 1.072\,M_\odot$, age $3.6^{+3.1}_{-2.3}$ Gyr) that is a member of a wide binary with a projected separation of 1030 au (Yee et al. 2023). Jankowski et al. (2025) showed that the planet may undergo tidal engulfment within ∼500 Myr for $Q'_\star < 10^7$ and within ∼1 Gyr for $Q'_\star \approx 10^8$, while no engulfment is expected within 5 Gyr for $Q'_\star \gtrsim 10^9$. Their TESS-based timing analysis revealed no statistically significant evidence for orbital decay or a perturber.

From our median models, we found $\Delta\mathrm{AIC} = 1.98$ and $\Delta\mathrm{BIC} = 5.05$, providing no significant evidence for a decaying orbit. Our median model for orbital decay claims a decreasing orbital period with a rate of -5 ± 11 ms yr^{-1}. Based on the measured orbital period change of TOI-1937A b, we place an upper limit on the stellar tidal quality factor of

$Q'_\star \lesssim 3.4 \times 10^9$ at the 95% confidence level. The lower limit is constrained by the physical requirement $Q'_\star > 0$ for tidal dissipation.

Our theoretical models of the star indicate that gravity waves would provide $Q'_{\rm IGW} \approx 2.33 \times 10^5$ at 3.6 Gyr, assuming the fully damped regime. This is likely to be valid as the critical planetary mass for wave breaking is only $0.75\,M_{\rm J}$, hence wave breaking is predicted and we would predict orbital decay to be occurring. This does not appear to be compatible with observations, so follow-up studies of this system would be worthwhile.

4.4.9. TOI-2109

TOI-2109 b ($M_{\rm p} = 5.02\,M_{\rm J}$, $R_{\rm p} = 1.347\,R_{\rm J}$) has one of the shortest orbital periods among known exoplanets, orbiting in only 0.67 day (∼16 hr), and is also among the hottest with $T_{\rm eq} = 3631$ K (Wong et al. 2021). This HJ orbits an F-type star with $M_\star = 1.447\,M_\odot$ and $T_{\rm eff} = 6500$ K and has therefore been widely considered a prime target for studying orbital decay and tidally driven atmospheric escape (Wong et al. 2021; Rosário et al. 2022; Weinberg et al. 2024). The likelihood of orbital decay was first evaluated by Wong et al. (2021), who predicted $\dot{P} \approx 10$–$740\,{\rm ms\,yr^{-1}}$ for $Q'_\star \approx 10^5$–10^7. Using recent TESS and CHEOPS data, Harre et al. (2024) reported tentative evidence for orbital decay after correcting the transit times with a sinusoidal TTV model, suggesting a nearby outer companion with $P_{\rm c} > 1.125$ days; however, confirmation is currently limited by the host star's rapid rotation and the lack of precise RV constraints.

From our analysis, we found that $\Delta{\rm AIC} = -1.16$ and $\Delta{\rm BIC} = 1.09$. Hence, we conclude that no statistically supported evidence for orbital decay has been found. From our quadratic model, we measured an orbital change of 26 ± 11 ms yr^{-1}. Again, using the 3σ lower limit of dP/dE, we constrain the modified stellar tidal quality factor $Q'_\star > (1.23 \pm 0.20) \times 10^6$.

The star probably rotates rapidly with an estimated rotation period of approximately $P_{\rm rot} = 2\pi R_\star (v \sin i)^{-1} = 1.14$ days adopting $v \sin i = 81.2\,{\rm km\,s^{-1}}$ (Wong et al. 2021). This is sufficiently fast that inertial waves may be excited in the stellar convective envelope. Our models for the star predict $Q'_{\rm IGW} \approx 1.2 \times 10^8$ for gravity waves (assuming the fully-damped regime, which is not expected to be valid as wave breaking is not predicted) at 1.77 Gyr, and $Q'_{\rm IW} \approx 6.9 \times 10^6$ at the same age due to inertial waves—which is compatible with the observational constraints. Thus, inertial waves are probably the dominant tidal mechanism in this system, and since $P_{\rm orb} < P_{\rm rot}$, we would predict orbital decay (and stellar spin-up) driven by these waves. Note that the value adopted here gives a representative value for inertial wave dissipation across the whole frequency range in which these waves can be excited, and the actual value we would expect for the tidal frequency of this system is more uncertain. (It could be larger or smaller, depending on the proximity of the tidal frequency to the frequency of the most dissipative inertial mode peaks in the response e.g., Ogilvie 2013; Astoul & Barker 2023.)

4.4.10. TrES-1

TrES-1 b ($M_{\rm p} = 0.752\,M_{\rm J}$, $R_{\rm p} = 1.067\,R_{\rm J}$; Torres et al. 2008) is one of the first exoplanets discovered by the transit method (Alonso et al. 2004) and therefore has the longest baseline in our orbital decay sample, with more than 20 yr of data. It orbits a K0 main-sequence star with $T_{\rm eff} = 5230$ K and $M_\star = 0.878\,M_\odot$ (Bonomo et al. 2017) in ∼3 days. Although it was not initially included due to its different location in parameter space (Figure 1), we manually involved this system given the extensive attention it has received in the literature. Early timing analyses found no significant TTVs (Rabus et al. 2009a; Baluev et al. 2015). After the inclusion of TESS data, Ivshina & Winn (2022) reported a period decrease of $-18.36 \pm 3.73\,{\rm ms\,yr^{-1}}$. Using extended ETD coverage, Hagey et al. (2022) found support for orbital decay with $\Delta{\rm BIC} = -9.7$ and $dP/dt = -10.9 \pm 2.1\,{\rm ms\,yr^{-1}}$. More recently, E. R. Adams et al. (2024) derived a decay rate of $-16.4 \pm 4.9\,{\rm ms\,yr^{-1}}$ over 2293 cycles ($\Delta{\rm BIC} = -68.8$), but inferred a physically implausible tidal quality factor of $Q'_\star = 160$.

From our timing analysis, we also found that the orbit is likely to be undergoing decay as the goodness of fit favors the quadratic model with $\Delta{\rm AIC} = -13.57$ and $\Delta{\rm BIC} = -11.02$. Our median quadratic model indicates a decrease in the orbital period of TrES-1 b with a rate of $-14.9 \pm 0.6\,{\rm ms\,yr^{-1}}$, in agreement with the previous work within the 95% confidence level. Similar to E. R. Adams et al. (2024), we infer a value of $Q'_\star = 570 \pm 60$, which is about three orders of magnitude lower (i.e., more efficient) than that of WASP-12 b and at least five orders of magnitude lower than the theoretical predictions of Weinberg et al. (2024), who estimated $Q'_\star > 10^7$. For comparison, WASP-12 is expected to be a subgiant star and exhibits efficient tidal dissipation via IGW (see 4.4.12). However, as indicated by E. R. Adams et al. (2024) too, there are no indications for TrES-1 to be in its subgiant phase. Therefore, although the observed timing variations are statistically significant, the inferred $Q'_\star$ is not in agreement with standard tidal dissipation models, and alternative mechanisms may be responsible for the observed signal.

Our theoretical models of TrES-1 indicate that gravity waves provide $Q'_{\rm IGW} \approx 2.57 \times 10^6$ at 3.7 Gyr. The critical planetary mass is $15.4\,M_{\rm J}$, suggesting that wave breaking is not predicted in the radiative core of the star. The star rotates too slowly for inertial waves to be excited for an aligned orbit and equilibrium tide dissipation is also predicted to be negligible. Hence, we would predict the orbit to be decaying slowly, with $Q'_{\rm IGW} \gtrsim 2.57 \times 10^6$, and possibly much more slowly than this unless the system is lucky enough to resonantly excite a *g*-mode. If this is the case, it is possible in principle for Q' to be smaller, though it is likely to be difficult to reconcile with the observational constraint.

There are two statistically significant peaks on the LS periodogram of the TTV data for TrES-1 b. The first one corresponds to 37.4 days and the second to 54.2 days with FAP values smaller than 0.01%. The potential companion at $13\overset{''}{.}16$ (Michel & Mugrauer 2024) cannot be the source of such a signal because it is too far away, although it is most probably gravitationally bound. A potential TrES-1 c has been suggested to cause an increase in the flux during a transit of TrES-1 b by Rabus et al. (2009b), and in a long-term variation in the radial velocities by Hagey et al. (2025), most recently, which cannot induce the observed TTVs due to its long period (~1200 days). However, neither claims were not supported by observational evidence as definite causes. Observations of flux variations due to magnetic activity have been reported, which might have caused a flux increase if brighter regions (faculae) were involved. Such magnetic activity-induced variations are also observed to affect RV observations. Hagey et al. (2025) investigated the potential of apsidal motion, but the amplitude of their TTV diagram can only be explained by the presence of an undetected close-in planetary companion because the orbit of TrES-1 b was found to be circular. Therefore, we think that both claims of potential companions and the statistically significant frequencies in our LS periodogram might be related to the same source, the magnetic activity of the star.

4.4.11. WASP-3

WASP-3 b ($M_{\rm p} = 1.89\,M_{\rm J}$, $R_{\rm p} = 1.42\,R_{\rm J}$; Bonomo et al. 2017) is a HJ orbiting a F7–8 type ($T_{\rm eff} = 6400$ K) main-sequence star (2.1 ± 1.2 Gyr; Southworth 2011) in 1.8 days, discovered by Pollacco et al. (2008), with a slightly misaligned orbit ($\lambda = 15^\circ \pm 10^\circ$; Simpson et al. 2010). The first discussion of the tidal evolution of the system was presented by Pont (2009). The system has been extensively monitored for orbital period variations. While some studies reported deviations from a constant period (Maciejewski et al. 2010; Eibe et al. 2012; Nascimbeni et al. 2013), others found no evidence for inner or outer perturbers (Montalto et al. 2012; Maciejewski et al. 2013, 2018a).

As a result of our TTV analysis, we found $\Delta{\rm AIC} = 1.32$ and $\Delta{\rm BIC} = 4.64$. Thus, we conclude that there is no evidence to indicate that the system is undergoing orbital decay. From our median quadratic model, we found $dP/dt = -1.6 \pm 0.8$ ms yr^{-1} and this corresponds to $Q'_\star > (3.8 \pm 1.3) \times 10^6$ at 95% confidence level.

Our theoretical models indicate that efficient gravity wave dissipation could provide $Q'_{\rm IGW} \approx 3.8 \times 10^7$ at 2.1 Gyr, in the fully-damped regime. The star has a convective core, so wave breaking is not predicted, making it uncertain whether the fully-damped regime is applicable (though magnetic wave conversion is another possibility).

4.4.12. WASP-12

WASP-12 b might be the only exception in our sample, as our primary goal was not to detect orbital decay itself, but to update relevant parameters and discuss the host star's tidal dissipative efficiency. First discovered by Hebb et al. (2009), WASP-12 b ($M_{\rm p} = 1.47\,M_{\rm J}$, $R_{\rm p} = 1.96\,R_{\rm J}$; Collins et al. 2017a) was the first exoplanet with observed tidal orbital decay. This HJ orbits a F9 star ($T_{\rm eff} = 6360^{+130}_{-140}$ K; Collins et al. 2017a) in 1.09 d. Maciejewski et al. (2016) reported a period decrease of $dP_{\rm orb}/dE = (-8.9 \pm 1.4) \times 10^{-10}$ d cycle^{-1}, confirmed by subsequent studies (Patra et al. 2017; Maciejewski et al. 2018b; Öztürk & Erdem 2019; Yee et al. 2020; Turner et al. 2021; Wong et al. 2022; Kutluay et al. 2023; Alvarado et al. 2024; E. R. Adams et al. 2024; Leonardi et al. 2024; Sodickson & Grunblatt 2025). Debate focuses on the host star's evolutionary state: Weinberg et al. (2017) and Barker (2020) suggest a subgiant to explain $Q'_\star \sim 10^5$ via wave breaking, whereas Duguid et al. (2024) argue magnetic wave conversion in a main-sequence star with a convective core could also explain the observed $Q'_\star$. Overall, our goal was to provide updated ephemerides and $Q'_\star$.

Building upon the previous arguments, our timing analysis also supports a decaying orbit for WASP-12 b, with $\Delta{\rm AIC} = -189.7$ and $\Delta{\rm BIC} = -186.25$. From our median quadratic fit, we calculated an orbital period decrease of -29.4 ± 4.0 ms yr^{-1}, which agrees with previous estimates within the 95% confidence level. Indeed, the most recent calculations by E. R. Adams et al. (2024) and Alvarado et al. (2024), found $dP/dt = -29.8 \pm 1.6$ ms yr^{-1} and $dP/dt = -29 \pm 2$ ms yr^{-1}, respectively. The corresponding modified stellar tidal quality factor is $Q'_\star = (1.72 \pm 0.18) \times 10^5$. In addition, we also fitted a cubic model to provide an estimate of the rate of tidal decay of WASP-12 b. Following Alvarado et al. (2024), the acceleration of the orbital period change in this model can be calculated from the cubic model, defined as

$$T(E) = T_0 + P_{\rm orb} \times E + \frac{1}{2}\frac{dP_{\rm orb}}{dE} \times E^2 + \frac{1}{6}\frac{d^2P_{\rm orb}}{dE^2} \times E^3, \tag{12}$$

and the corresponding rate of change of the rate of tidal decay is analytically provided as

$$\ddot{P} \approx 1.2 \times 10^{-24}\ {\rm s}^{-1}\left(\frac{Q'_\star}{10^6}\right)^{-1}\left(\frac{M_{\rm p}}{M_{\rm J}}\right)\left(\frac{M_\star}{M_\odot}\right)^{-8/3} \times \left(\frac{R_\star}{R_\odot}\right)^{5}\left(\frac{P}{\rm d}\right)^{-13/3}\left(\frac{\dot{P}}{10^{-9}}\right). \tag{13}$$

Again, we followed the same methodology described in Section 4.2 while implementing the probabilistic fitting. Our cubic fit is displayed in Figure 5. From our median acceleration model, we found that $d^2P_{\rm orb}/dE^2 = (-3.81 \pm 0.52) \times 10^{-13}\,{\rm d\ cycle^{-2}}$. Hence, the corresponding acceleration of orbital decay in WASP-12 b is $\dddot{P} \approx -4.29 \times 10^{-23}\ {\rm s^{-1}}$, which is slightly faster than what Alvarado et al. (2024) found earlier. This difference might be considered quite negligible when the change is also negligibly small, so we consider our results to be consistent with those of Alvarado et al. (2024).

From our theoretical models (Figure 7), we find that IGWs can provide $Q'_\star \approx 10^5$ for an age of approximately 3.0 Gyr for all models with stellar masses of $\{1.30, 1.35, 1.434\}\,M_\odot$ and metallicities of $\{0.1, 0.2, 0.3\}$ dex. The predicted critical planetary mass at this age appears to be lower than the observed value of $M_{\rm p} = 1.47\,M_{\rm J}$ (Collins et al. 2017a). Our models, therefore, suggest that the host star should currently be in its subgiant phase in order to reproduce the observed value $Q'_\star = (1.72 \pm 0.18) \times 10^5$, consistent with the findings of Barker (2020). Alternatively, Duguid et al. (2024) showed that the same fully-damped regime for gravity waves can be explained by magnetic wave conversion even if the star is a main-sequence star with a convective core, which remains another possibility for this system. On the other hand, IWs are not expected to be excited (by the asynchronous tide with $l = m = 2$) in the convective zone because the stellar rotation period is $P_{\rm rot} = 37.4$ days, as inferred from $v \sin i = 2.2\ {\rm km\,s^{-1}}$ (Bonomo et al. 2017) and does not satisfy the criteria mentioned in Section 1.

4.4.13. WASP-19

WASP-19 b ($M_{\rm p} = 1.154\,M_{\rm J}$, $R_p = 1.415\,R_{\rm J}$; Cortés-Zuleta et al. 2020) was the shortest-period exoplanet when it was discovered (Hebb et al. 2010) and is the second shortest in our sample after TOI-2109 b, making it a strong candidate for tidally-driven orbital decay. It orbits a G8 star ($T_{\rm eff} = 5616$ K, $M_\star = 0.965\,M_\odot$, $R_\star = 1.006\,R_\odot$) in 0.78 d, with a well aligned orbit ($\lambda = -4\overset{\circ}{.}6 \pm 5\overset{\circ}{.}2$; Hellier et al. 2011). Since discovery, the orbital decay scenario has been probed extensively (e.g., Mancini et al. 2013b). Petrucci et al. (2020) found a linear ephemeris favored the quadratic model with $Q'_\star > (1.23 \pm 0.23) \times 10^6$. Reported period changes vary: -6.5 ± 1.3 (Patra et al. 2020) and $-3.7 \pm 0.5\ {\rm ms\ yr^{-1}}$ (Korth & Parviainen 2023). Maciejewski et al. (2024) found no significant signal, but Sodickson & Grunblatt (2025) reported $-3.89 \pm 0.37\ {\rm ms\ yr^{-1}}$. Recent studies favor apsidal motion ($\Delta{\rm BIC} = -370.4$; Biswas et al. 2024) and we will discuss this scenario in Section 5.1.

Our median models yielded $\Delta{\rm AIC} = 1.96$ and $\Delta{\rm BIC} = 5.63$, providing no evidence of decreasing or increasing orbital period over time. Using the 1.96σ lower limit on the quadratic coefficient is $a_{\rm lower} = -6.884 \times 10^{-12}\ {\rm d\ cycle^{-1}}$, we provide $Q'_\star > 5.0 \pm 0.7 \times 10^6$ at 95% confidence level.

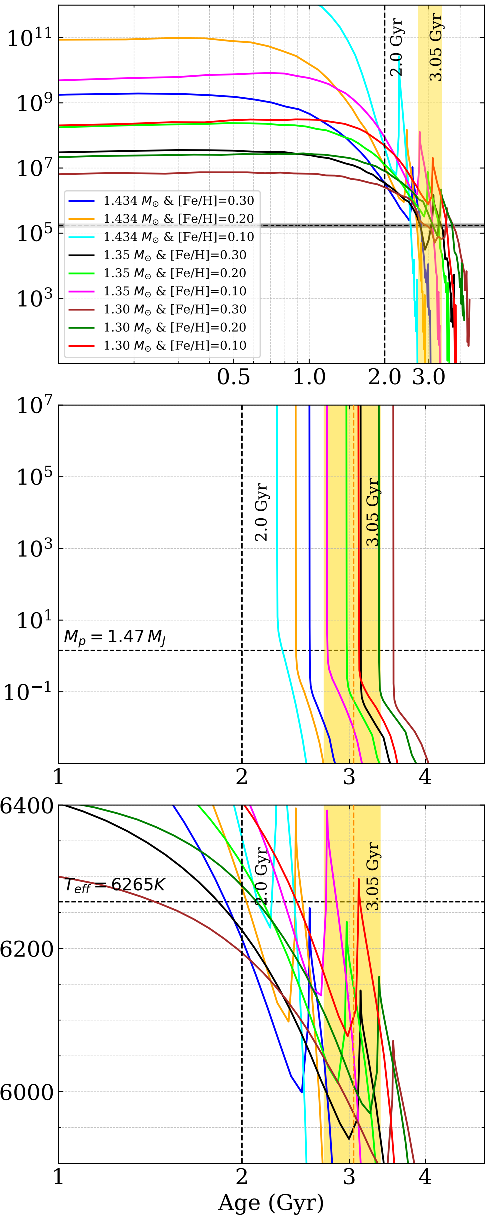

Figure 7. Top: WASP-12's tidal efficiency due to IGW ($Q'_{\rm IGW}$) as a function of stellar age for 9 different stellar evolution models. The dashed horizontal line displays $Q'_\star = 1.72 \times 10^5$ from our median quadratic model. Middle: Critical mass of WASP-12 b for wave breaking in the stellar core $M_{\rm crit}$ as a function of stellar age. The horizontal dashed line shows the planetary mass $M_{\rm p} = 1.47\,M_{\rm J}$ from Collins et al. (2017a). Bottom: WASP-12's stellar effective temperature $T_{\rm eff}$ as a function of stellar age. Here, dashed horizontal line shows $T_{\rm eff} = 6265$ K from Leonardi et al. (2024). For each plot, we show the age reported by Collins et al. (2017a) (2.0 Gyr) as a vertical black dashed line, and the age from Leonardi et al. (2024) (3.05 $\pm$ 0.22 Gyr) as an orange dashed line at the nominal value. The gold-shaded region represents the 68% confidence interval.

Our theoretical models of WASP-19 predict that fully-damped gravity waves provide $Q'_{\rm IGW} \approx 6 \times 10^4$ for ages of approximately 6 Gyr (ranging from 8×10^4 to 5×10^4 for ages between 3 and 7 Gyr, respectively). The critical planetary mass for wave breaking passes below $1\,M_J$ for stellar ages of approximately 6 Gyr. This indicates that the fully damped regime is very likely for ages older than this, as this value exceeds the planetary mass. It is therefore difficult to explain the inferred $Q'_\star > 5 \times 10^6$ unless the stellar age is less than 6 Gyr. The critical mass is as large as $10\,M_J$ for 3 Gyr ages, decreasing to $1\,M_J$ by 6 Gyr. We can therefore plausibly explain the observational constraint if the star is younger than 6 Gyr. Inertial waves cannot be excited by an aligned orbit, and equilibrium tide damping is likely to be negligible. This theoretical interpretation is very similar to the one presented in Barker (2020).

WASP-19 b's orbit was found to be slightly eccentric ($e = 0.0126^{+0.0140}_{-0.0089}$; Cortés-Zuleta et al. 2020). Biswas et al. (2024) proposed that its apsidal motion is causing TTVs, which might be amplified by magnetic activity. Recent studies have not found any outside perturber (Petrucci et al. 2020; Sodickson & Grunblatt 2025) that would cause the observed TTVs. We found a significant periodicity at 16.75 d, which can only be associated with the magnetic activity of the star. Some of the transit light curves of WASP-19 b are heavily affected by starspot-induced asymmetries. Out-of-transit variability is evident in the TESS light curves as well. When the data are pre-whitened from this peak, another peak is observed at lower frequencies, corresponding to ∼1536 d. However, our sinusoidal fits with this periodicity do not compete with the linear model in terms of fit statistics. When we phase-fold the data with the periodicity, we do not observe a good agreement with the sinusoidal model either. Nonetheless, we report these frequencies for future work on the TTVs of the target.

4.4.14. WASP-46

WASP-46 b ($M_p = 1.91\,M_J$, $R_p = 1.174\,R_J$; Ciceri et al. 2016) is an HJ orbiting a G6 star ($T_{\rm eff} = 5600$ K) in a 1.43 days circular orbit, discovered by Anderson et al. (2012). The host star shows chromospheric activity, allowing age estimates of 1.5 Gyr (Anderson et al. 2012) and later 9.6 Gyr (Ciceri et al. 2016; Bonomo et al. 2017). For the investigation of orbital decay, Petrucci et al. (2018) used 6 yr of photometry and found that orbital decay model favors (ΔBIC = −5.0) with a stellar tidal quality factor $Q'_\star > 7 \times 10^3$ from $\delta P = -0.12 \pm 0.45$ ms yr^{-1}. Adams et al. (2024), using nearly 14 yr of data, found a period increase of 21.6 ± 8.2 ms yr^{-1}, but after rescaling errors and removing outliers, ΔBIC = 2.0. This highlights the need for further observations because the early light-curve data are not of high quality.

Our timing analysis resulted in ΔAIC = −1.13 and ΔBIC = 1.36. Therefore, in agreement with Petrucci et al. (2018) and Adams et al. (2024), we also found no significant evidence for orbital decay signal in TTV data. From the median orbital decay model, the 3σ period derivative values are 1.71×10^{-10} d cycle^{-1} and 3.10×10^{-10} d cycle^{-1}. Since both values are positive, the corresponding tidal quality factors would be negative. Because $Q'_\star$ must be physically positive (for tidal dissipation rather than anti-dissipation), no meaningful 3σ lower or upper limit can be derived from our analysis.

Our theoretical models for the host star find $Q'_{\rm IGW} \approx 2.58 \times 10^5$ for gravity waves in the fully-damped regime at 9.6 Gyr. We estimate that the critical planetary mass for wave breaking is $1.7\,M_J$ at the same age, which is slightly lower than the mass of the planet, indicating that wave breaking is predicted—though this is marginal. We would predict orbital decay at a rate consistent with $Q'_{\rm IGW} \gtrsim 2.58 \times 10^5$, with the lower limit achievable if the waves are fully damped.

4.4.15. WASP-87

WASP-87 b is a HJ orbiting a metal-poor ([Fe/H] = −0.41 ± 0.10) mid-F star ($T_{\rm eff}$ = 6250 ± 110 K) with $P_{\rm orb}$ = 1.68 d (Anderson et al. 2014). Rossiter–McLaughlin observations indicate a nearly aligned orbit ($\lambda = -8^\circ \pm 11^\circ$; Addison et al. 2016), and the host star has a rotation period of ∼8.6 days. The system has a Sun-like companion, WASP-87 B, with both stars having similar ages (3.8 ± 0.8 and 3.8 ± 0.6 Gyr; Anderson et al. 2014). Spitzer occultation observations confirm a circular orbit (Garhart et al. 2020). WASP-87 lies in the sparsely populated $P_{\rm rot}$–$P_{\rm orb}$ region (McQuillan et al. 2013), potentially shaped by tidal interactions.

As a result, the 3σ period derivative values are 2.34×10^{-10} and 2.14×10^{-9}, both in d cycle^{-1} unit. Since both values are positive, the corresponding tidal quality factors would be negative. Because $Q'_\star$ must be positive, no meaningful 3σ lower or upper limit can be derived from these data. We detect no significant TTVs but, by updating the ephemeris, we note that the bright, hot host star makes the system a good target for atmospheric studies at shorter wavelengths (Cauley et al. 2017).

Our theoretical models predict $Q'_{\rm IGW} \approx 4.5 \times 10^6$ at 1 Gyr, due to gravity wave dissipation if these waves are fully damped. However, wave breaking is not predicted in the star, probably making this a lower bound on $Q'_\star$.

4.4.16. WASP-103

WASP-103 b is one of the hot Jupiters in our sample with an orbital period shorter than one day, and it has received considerable attention since its discovery by Gillon et al. (2014). Although the system lies near the ecliptic and therefore lacks TESS coverage, ground-based efforts have provided a nearly uninterrupted and long-term observational baseline up to the present day. Baştürk et al. (2022) first investigated the possibility of a changing orbital period but found no evidence. Similarly, Maciejewski et al. (2022) found ΔBIC = 3.0 and

Barros et al. (2022) stated that the linear ephemeris is preferable for the current set of light curves. The most recent attempt came from Alvarado et al. (2024) but again no compelling evidence supporting a period variation was reported.

As in previous studies, our analysis also fails to identify a statistically preferable model for a changing orbital period. From our median quadratic model, we find $\dot{P} = -2.0 \pm 0.7$ ms yr^{-1} and we derive a lower limit of $Q'_* > (1.83 \pm 0.17) \times 10^6$ at the 95% confidence level.

Our theoretical models predict $Q'_{\rm IGW} \approx 1.8 \times 10^6$ at 1.7 Gyr due to gravity waves, which is remarkably close to the observational lower limit. Wave breaking is not predicted though, so this is probably a lower bound on the dissipation due to gravity waves, unless the system happens to excite a g-mode in resonance.

4.4.17. WASP-114

WASP-114 b is a neglected planet in terms of its potential to display orbital decay, although it is a massive (1.769 $M_{\rm J}$) planet on a very short-period ($P_{\rm orb}$ = 1.5488 days) orbit (Barros et al. 2016). Patra et al. (2020) constructed the first ever TTV diagram with only two data points spanning less than a thousand epochs. Later Kokori et al. (2022), Ivshina & Winn (2022), and Kokori et al. (2023) only updated its linear ephemerides.

From our median models, we found ΔAIC = −0.56 and ΔBIC = 0.94. Therefore, we concluded that from the TTV analysis, there is no statistically significant evidence for a changing orbital period. From our median quadratic model, we found a decreasing orbit with a rate of -35 ± 10 ms yr^{-1}. So, we used this value to constrain stellar tidal quality factor and we provide $Q'_* > 4.7 \pm 0.6 \times 10^6$ at the 95% confidence level.

Our theoretical models predict $Q'_{\rm IGW} \approx 4.8 \times 10^3$ at 4.3 Gyr due to gravity waves. Since the star is likely to be a post-MS star, perhaps in the sub-giant phase, the star has a radiative core and wave breaking is predicted for the planetary mass, as $M_{\rm crit} < 0.1\, M_{\rm J}$ by the estimated age of the star. Hence, we predict orbital decay for the planet at a rate consistent with $Q'_{\rm IGW} \approx 4.8 \times 10^3$, though the precise value is sensitive to stellar age during this phase of the star's evolution. For the models we have considered, the theoretical predictions appear to be in conflict with the observational constraint, though the predictions do depend strongly on stellar age.

4.4.18. WASP-121

WASP-121 b attracted attention because it exhibited a radius anomaly (1.865 $R_{\rm J}$ for 1.183 $M_{\rm J}$) and also due to its proximity to the Roche limit, which is only 1.15 times its current orbital separation (Delrez et al. 2016). Salz et al. (2019) reported tentative (1.9σ) ultraviolet absorption of 0.55%, potentially due to atmospheric mass loss, similar to WASP-12 b (Fossati et al. 2010), and Yan et al. (2021) derived a mass-loss rate of 1.28×10^{12} g s^{-1}. The planet has an almost polar orbit (Bourrier et al. 2020), which is possibly linked to its late arrival and minimal damping of orbital obliquity (Spalding & Winn 2022). Maciejewski (2022) compiled mid-transit times from literature and TESS Sectors 7, 33, and 34, showing no departure from linear ephemerides. E. R. Adams et al. (2024) analyzed 66 data points and noted that only the earliest composite point suggested a period increase. Finally, Sing et al. (2024) measured a dynamical mass of 1.170 ± 0.043 $M_{\rm J}$ from planetary atmospheric Doppler shifts.

From our analysis, we found ΔAIC = −16.82 and ΔBIC = −13.84, meaning a statistically significant preference for the quadratic model. The median quadratic model provides a secular increase in the orbital period with $dP_{\rm orb}/dt = 15.1 \pm 0.8$ ms yr^{-1}. Since the stellar spin is faster than the planetary orbit ($P_{\rm orb}$ = 1.27 days; Table 1 and $P_{\rm rot}$ = 1.15 days; Table 5), the orbital growth might be a viable explanation for this result. Lastly, we could not provide a constraint on $Q'_\star$, as both limits of $\dot{P}$ resulted in a positive value.

Our theoretical models for WASP-121 indicate that the most efficient tidal mechanism is likely to be inertial waves, with a typical value $Q'_{\rm IW} \approx 6.6 \times 10^6$ at 1.5 Gyr. Gravity waves are predicted to be less effective, with $Q'_{\rm IGW} \approx 1.48 \times 10^{10}$ at the same age, and wave breaking is not predicted in the star. The star rotates with a period of $P_{\rm rot} \approx 1.13$ days (Bourrier et al. 2020), indicating that inertial waves will be excited in the convective envelope and we also expect outward migration due to these waves, since $P_{\rm rot} < P_{\rm orb}$.

4.4.19. WASP-122 (KELT-14)

WASP-122 b (or KELT-14 b) is an important candidate for displaying orbital decay because it orbits a G2 star near the main sequence turnoff (Rodriguez et al. 2016). Previous studies have noted its potential for orbital decay (Patra et al. 2020) and compiled transit timings from the literature and TESS observations (Shan et al. 2023; Maciejewski 2022), but none found evidence for deviations from a linear ephemeris. Rossiter-McLaughlin observations indicate that the orbit is circular and well-aligned (Stangret et al. 2024).

From our TTV analysis, we found ΔAIC = −1.13 and ΔBIC = 1.32. Therefore, we conclude that there is no statistically significant preference for any model. Our median quadratic model suggests that the 99.7% confidence-level lower limit of $a_1^{\rm lim} = -2.822 \times 10^{-10}$ d cycle^{-1} corresponds to $Q'_\star > (4.6 \pm 0.5) \times 10^4$.

Our theoretical models of WASP-122 predict that gravity waves (in the fully-damped regime) can provide $Q'_{\rm IGW} \approx 1.1 \times 10^7$ at 1.44 Gyr. The planet is unlikely to cause these waves to break though magnetic wave conversion is a

Table 5
Stellar Properties Related to the Efficient IW and IGW Dissipation for the Systems in Our Sample

System	Age (Gyr)	$P_{\rm rot}$[b] (days)	$v \sin i$ (km $\rm s^{-1}$)	$Q'_{\rm IW}$	$Q'_{\rm IGW}$	$M_{\rm crit}$[c] ($M_{\rm J}$)	Wave breaking?	References[a]
CoRoT-2	2.7	4.48	11.85	⋯	1.94×10^6	1.4	Yes	(1)
HAT-P-23	4	7.01	8.10	⋯	6.7×10^5	⋯	No	(2)
HATS-18	4.4	9.8	6.23	⋯	1.2×10^5	$\sim$1	Yes	(3)
KELT-9	0.3	0.79	111.40	$\sim 10^{10}$	$\sim 10^{12}$	⋯	No	(4)
KELT-16	2	9.05	7.6	⋯	1.5×10^6	⋯	No	(5)
Qatar-1	11.6	28	1.70	⋯	1.85×10^5	0.5	Yes	(1)
Qatar-4	0.15	6.0	7.1	⋯	1.63×10^6	$\gtrsim 10^3$	No	(6)
TOI-1937A	3.6	6.5	⋯	⋯	2.33×10^5	0.75	Yes	(7)
TOI-2109	1.77	1.14	81.2	6.9×10^6	1.2×10^8	⋯	No	(8)
TrES-1	3.7	31.4	1.3	⋯	2.57×10^6	15.4	No	(1)
WASP-3	2.1	5.15	13.4	⋯	3.8×10^7	⋯	No	(1)
WASP-12	3.05	37.4	2.2	⋯	1×10^5	0.1	Yes	(1)
WASP-19	6	10.5	4.0	⋯	6×10^4	1.0	Yes, for older stars	(1)
WASP-46	9.6	16.0	1.9	⋯	2.58×10^5	1.7	Yes, marginally	(1)
WASP-87	?	30	9.9	⋯	4.5×10^6	⋯	No	(9)
WASP-103	1.7?	6.85	10.6	⋯	1.8×10^6	⋯	No	(1)
WASP-114	4.3	6.85	6.4	⋯	4.8×10^3	< 0.1	Yes	(10)
WASP-121	1.5	1.13	13.5	6.6×10^6	1.48×10^{10}	⋯	No	(11)
WASP-122	1.44	$\sim$30	3.3	⋯	1.1×10^7	⋯	No	(12)
WASP-167	1.3	1.88	⋯	6.5×10^9	4×10^{14}	⋯	No	(13)

Notes.
[a] Reference for $P_{\rm rot}$ or $v \sin i$.
[b] For the stars whose $P_{\rm rot}$ has not been provided by previous literature sources, we used the simple formula of $P_{\rm rot} = 2\pi R_\star / v \sin i$.
[c] We indicate all stars with convective cores using "-" since wave breaking is not predicted in them.
References: 1. Bonomo et al. (2017), 2. Salisbury et al. (2021), 3. Penev et al. (2016), 4. Gaudi et al. (2017), 5. Oberst et al. (2017), 6. Alsubai et al. (2017), 7. Jankowski et al. (2025), 8. Wong et al. (2021), 9. Addison et al. (2016), 10. Addison et al. (2016), 11. Delrez et al. (2016), 12. Turner et al. (2016), 13. Temple et al. (2017).

possibility to justify this fully damped regime, particularly if the star is near the end of the MS or older (Duguid et al. 2024). The star probably rotates far too slowly for inertial waves to be excited. Lastly, it should be noted that the estimated age from Turner et al. (2016) is approximately 5 Gyr older than what we present for efficient IGW dissipation in the fully-damped regime, though the prior age constraint may be unreliable.

4.4.20. WASP-167 (KELT-13)

WASP-167 b is a neglected hot-Jupiter in the literature although it has been over eight years since its discovery (Temple et al. 2017). It orbits an F1-type main-sequence star, which is a γ-Doradus pulsator (Kálmán et al. 2024). Kokori et al. (2023) and Kokori et al. (2022), Ivshina & Winn (2022), and Kokori et al. (2023) revised its ephemeris information but did not note any departure from the linear ephemerides.

From our timing analysis, we found an increasing period with a rate of 11.8 ± 4.1 ms $\rm yr^{-1}$. However, since the corresponding ΔAIC and ΔBIC do not exceed the threshold of 10, these findings are not statistically significant. Additionally, by adopting the 99.7% (3σ) confidence level upper limit for dP/dt, we provide a lower limit on $Q'_\star > (10.9 \pm 1.1) \times 10^7$.

Our theoretical models of WASP-167 indicate that gravity waves are probably inefficient, with $Q'_{\rm IGW} \gtrsim 10^{14}$ at 1.3 Gyr. On the other hand, the rapid rotation of the star, $P_{\rm rot} = 1.88$ days (Temple et al. 2017) implies that inertial waves are likely to be excited in the stellar convective envelope. Since $P_{\rm rot} < P_{\rm orb}$, it is likely that these waves would drive outward planetary migration, though our models predict $Q'_{\rm IW} \approx 6.5 \times 10^9$ at 1.3 Gyr as a representative value for the dissipation of these waves. Hence, tidally-driven orbital evolution is predicted to be very slow and unlikely to be detected according to our current theoretical understanding.

5. Discussion

5.1. Apsidal Motion Scenario

Apart from the constant period or secularly changing orbital period model, tidally induced apsidal precession is an alternative explanation for such TTV signals (e.g. Barker et al. 2024). For the systems with even a slight eccentric orbit, tidally induced apsidal precession produces quasi-periodic variations in the transit and occultation times. This mechanism has been discussed for several HJs in previous studies (e.g., KELT-9 b; Harre et al. 2023, WASP-19 b; Biswas et al. 2024).

Being motivated by these previous attempts, we followed the formalism from Harre et al. (2023) to test the apsidal motion hypothesis for nine HJs in our sample. For the rest of the sample, previous works have either ruled out the apsidal motion scenario or provided a circular orbit followed by subsequent measurements. Briefly, the apsidal precession model assumes a non-zero eccentricity and is defined as

$$t_{\mathrm{tra}}(N) = t_0 + EP_s - \frac{eP_a}{\pi}\cos\omega(E), \tag{14}$$

where

$$\omega(E) = \omega_0 + \frac{d\omega}{dE}E, \tag{15}$$

and

$$P_s = P_a\left(1 - \frac{1}{2\pi}\frac{d\omega}{dE}\right). \tag{16}$$

Here, P_s is the sidereal period, P_a is the anomalistic period and ω is the argument of periastron. We present our results with a ΔBIC compared to the constant period model in Table A9. That is, we replaced the quadratic model with apsidal motion model in Equation (10). Despite the physical plausibility of the mechanism, we have found no statistically significant evidence for apsidal precession. For all fits, $\Delta BIC > 140$ and is consistent with a circular orbit at 99.7% confidence level.

Several of the previously reported eccentricities or findings on the apsidal motion models in the literature are themselves subject to significant uncertainties and, in some cases, contradictory results. Small eccentricities inferred from RV measurements are particularly vulnerable to degeneracies between eccentricity and argument of periastron, as well as to the influence of stellar jitter and correlated noise (Shen & Turner 2008). It is therefore possible that at least some of the systems in our sample are in fact on nearly circular orbits, possibly as a result of tidal circularization (Valsecchi & Rasio 2014), in which case apsidal motion would not produce a measurable transit timing signal. Tidal circularization is usually thought to be primarily produced by dissipation inside the planet rather than the star (e.g. Ogilvie 2014; Lazovik et al. 2024). Gillon et al. (2010) reported a statistically significant eccentricity value of $0.0143^{+0.0077}_{-0.0076}$ for CoRoT-2 b's orbit by constraining the quantity $e\cos\omega$ with the help of Spitzer occultation observations. Therefore, an apsidal motion can be expected, but the relatively low precision of the Spitzer occultation timings prevents us from investigating this possibility in detail. For WASP-3 b, the orbit had been reported to be eccentric based on occultation (Rostron et al. 2014) and RV observations (Knutson et al. 2014; Bonomo et al. 2017). For HAT-P-23 b, Spitzer secondary-eclipse measurements suggest a circular orbit (O'Rourke et al. 2014), indicating past tidal circularization and alignment (e.g. Valsecchi & Rasio 2014); however, this is contradicted by the result of Stassun et al. (2017), who found $e = 0.11 \pm 0.04$. Although Gaudi et al. (2017) suggested a circular orbit for KELT-9 b's orbit, Harre et al. (2023) showed that the apsidal motion model better fit the data with $\Delta\mathrm{BIC} = -13.28$, so we considered this case as well. In order to test this mechanism for all systems, we encourage further occultation and radial velocity observations with adequate precision for eccentricity measurements and mid-occultation timings, which will vary in the opposite phase of the mid-transit timings in the presence of apsidal motion.

5.2. Comparison to the Previous Theoretical Results

For the hosts of exoplanets on tight ($a < 0.05$ au) and eccentric orbits, Bonomo et al. (2017) proposed $6 < \log_{10} Q'_\star < 7$ by comparing the circularization times of HJs and their host stars. This inferred interval is in agreement with some of our systems for which strictly circular orbits are not explicitly stated (Table A9). To specify, either observational limits or theoretical expectations lie within the specified range for CoRoT-2, HAT-P-23, HATS-18, KELT-9, TOI-2109, WASP-19, WASP-114 and WASP-167. However, this agreement is somewhat puzzling for these systems, since wave breaking is also expected to trigger efficient IGW dissipation for some of the host stars when the host star is approaching the terminal stage of the main sequence phase or has already entered the subgiant phase (Barker 2020). These two expectations do not appear to be fully consistent with each other, as the circularization timescale τ_c should be smaller than the inspiral timescale τ_a, otherwise we would not be able to see these objects in their current orbits (Ogilvie 2014). This might be the result of tidal dissipation inside the planet dominantly driving the circularization, instead of dissipation inside the star.

One of the most recent estimates was provided from Hamer & Schlaufman (2019), where they found that HJs with a mass of $1\,M_\mathrm{J} < M_\mathrm{p} < 2\,M_\mathrm{J}$ and an orbital period of $2\,\mathrm{days} < P_\mathrm{orb} < 5\,\mathrm{days}$ should satisfy $Q'_\star \lesssim 10^7$. This limit appears as the upper bound of the proposed value from Bonomo et al. (2017). If we also extend this estimate to our sample of HJs with $P < 2$ days, it can be concluded that the majority of our results estimates from timing analysis and theory are in approximate agreement with this value. Only the inferred Q'_IW for KELT-9 and WASP-167 exhibits a weaker dissipation by at least 2 orders of magnitude.

5.3. A Sanity Check for Tidal Stability

Following Hut (1980) (see also Levrard et al. 2009 and Matsumura et al. 2010), we also performed an additional check of the "stability" of the systems in our sample. If the total angular momentum (L_tot; the sum of the rotational L_spin and orbital L_orb components) of a system is smaller than a critical value (L_crit), i.e., $L_\mathrm{tot} < L_\mathrm{crit}$, then we say that the system is "Darwin unstable" and the HJ will spiral into the star to reach the Roche limit. On the other hand, if $L_\mathrm{tot} > L_\mathrm{crit}$, there are two

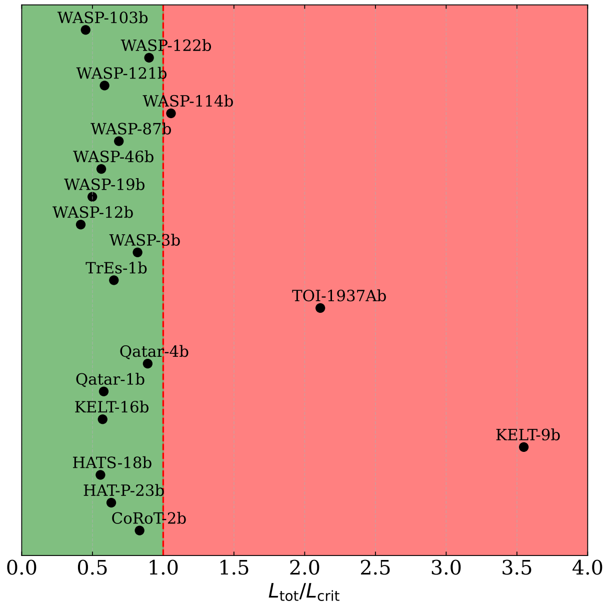

Figure 8. The ratio of the total angular momentum $L_{\rm tot}$ to the critical angular momentum $L_{\rm crit}$ for the studied HJ systems. The green region corresponds to $L_{\rm tot}/L_{\rm crit} < 1$, where the system is "Darwin unstable," while the red region corresponds to the $L_{\rm tot}/L_{\rm crit} > 1$, where the stability of the system depends on the relationship between $L_{\rm orb}$ and $L_{\rm spin}$.

outcomes: (1) $L_{\rm orb} < 3L_{\rm spin}$ (or $L_{\rm orb}/L_{\rm spin} < 3$) then the HJ will spiral into its star to reach the Roche limit, or (2) $L_{\rm orb} > 3L_{\rm spin}$ and the orbit is "stable," such that the planet will not spiral inward to reach the Roche limit. To infer which outcome we should expect in our systems if the total angular momentum is conserved, we first calculated the total angular momentum $L_{\rm tot}$ and the critical angular momentum $L_{\rm crit}$, which are defined by

$$L_{\rm tot} = \underbrace{C_\star \omega_\star}_{=L_{\rm spin}} + \underbrace{\frac{M_{\rm p} M_\star}{\sqrt{M_{\rm p} + M_\star}} \sqrt{Ga(1 - e^2)}}_{=L_{\rm orb}}, \tag{17}$$

and

$$L_{\rm crit} = 4\left[\frac{G^2}{27}\frac{M_\star^3 M_{\rm p}^3}{M_\star + M_{\rm p}}(C_\star + C_{\rm p})\right]^{\frac{1}{4}}, \tag{18}$$

where G is the gravitational constant, $C_\star = k_\star M_\star R_\star^2$ is the moment of inertia of the star, where $M_\star$ is the stellar mass, with $C_{\rm p}$ and $M_{\rm p}$ for the planet defined similarly, a is the semi-major axis and e is the eccentricity. We adopted $k_\star = 0.06$ for the host stars (e.g. Claret & Gimenez 1989) and $k_p = 0.26$ for the HJs in our sample (e.g. Gu et al. 2003; Lanza 2020). The results are displayed in Figure 8. Only three HJ systems (KELT-9, TOI-1937A and WASP-114 b) have $L_{\rm tot} > L_{\rm crit}$, such that there is currently enough angular momentum in the system for a stable tidal equilibrium state to exist in the absence of angular momentum loss due to stellar magnetic braking. For the remaining 17 systems, each one is predicted to have insufficient angular momentum for a stable equilibrium state to exist, and hence these planets are expected to spiral into their stars to destruction. However, the red region in Figure 8 does not necessarily imply that the orbit is stable, so we also checked which portion of the parameter space these 3 HJ systems occupy according to the relation between $L_{\rm orb}$ and $L_{\rm spin}$. For KELT-9 b, TOI-1937A b and WASP-114 b, we found $L_{\rm orb}/L_{\rm spin} = 0.11$, $L_{\rm orb}/L_{\rm spin} = 0.08$ and $L_{\rm orb}/L_{\rm spin} = 0.07$, respectively. Therefore, we conclude that all the HJs in our sample are "Darwin unstable," so we expect these planets to be engulfed after they have spiraled inside the Roche radius of their host-stars.

It should be remembered that angular momentum loss from the star-planet system, such as by stellar magnetic braking, will preclude an ultimate tidal equilibrium state in any of these systems even if the above criterion would have otherwise predicted them to be "stable" (e.g. Barker & Ogilvie 2009; Damiani & Lanza 2015; Barker 2025). Nevertheless, this check is useful for interpretation for cases where this angular momentum loss is expected to be weak, such as in the more massive stars in our sample, in particular KELT-9.

6. Conclusion

In this work, we first performed a target selection process to select the most suitable targets to investigate the orbital decay of HJs. We selected 20 systems with HJs and presented 42 new ground-based observations for 12 of these. With the help of measurements from ETD, TESS and the literature, we have investigated the likelihood of tidally driven orbital decay in each of these 20 HJ systems by exploring the significance of an orbital decay model in each system's TTV diagram. We fitted a linear (constant orbital period) model to each one and an apsidal motion model to those with eccentric orbits. We complemented this analysis with theoretical models of the stellar tidal dissipation.

We were able to confirm and update the parameters for the orbital decay of WASP-12 b, which has been extensively studied for over a decade. We have also confirmed that either WASP-12 should be in a subgiant phase to satisfy the observationally inferred $Q'_* \approx 10^5$ in theoretical models, or that magnetic wave conversion is in operation if WASP-12 is a main-sequence star (Duguid et al. 2024).

Additionally, our timing analysis has revealed statistically-favored orbital period changes for TrES-1 b and WASP-121 b. We have found that the orbital period is decreasing at a rate of -14.9 ± 0.6 ms yr^{-1} for TrES-1 b and increasing at a rate of 15.1 ± 0.8 ms yr^{-1} for WASP-121 b. TrES-1 b's decay implies very efficient stellar tidal dissipation with $Q'_* = 5.7 \times 10^2$, which is incompatible with our theoretical models. For this system, we do not predict gravity waves to break in the radiative core of the host star, and $Q'_\star$ is predicted to be four orders of magnitude larger when gravity waves are fully damped. Also, when we compare this inferred Q'_* with cases of WASP-12 b (Section 4.4.12) and WASP-4 b (Baştürk et al. 2025), we find that the outcome of TTV analysis does not agree with the expectations for similar systems. On the contrary, inertial waves can provide efficient tidal dissipation in the convective envelope of WASP-121, and are expected to cause orbital growth, consistent with the results of our timing analysis.

Apart from these three systems, our timing analysis indicates no significant evidence in favor of either a decaying or growing orbit in the remaining systems in our sample. Nevertheless, for almost half of the planets in our list, wave breaking of gravity waves in the stellar radiative core is expected and should lead to efficient gravity wave dissipation. For those in which wave breaking is not expected, such as in hotter stars with convective cores, magnetic wave conversion is an alternative explanation to provide efficient damping of gravity waves and the resulting Q'_* (Duguid et al. 2024). Another argument to motivate monitoring these objects further is that all of these systems are “Darwin unstable,” meaning that eventually the HJ will migrate towards the Roche limit of its host star. Therefore, we believe that our work could motivate future follow-up studies of these systems. At least half of the systems in our sample will be observed by TESS in 2026 or 2027. In addition, the PLATO mission is expected to be launched before the end of 2026 (Rauer et al. 2025). WASP-121, WASP-122, TOI-1937A, and other systems with potential but not in our sample lie within the LOPS2 field (Nascimbeni et al. 2025). Thus, we expect further observational constraints to be imposed on the tidal quality parameters of the hosts of these systems and therefore to obtain a better understanding of tidal interactions in the coming years.

Acknowledgments

We gratefully acknowledge the support of the Scientific and Technological Research Council of Türkiye (TÜBİTAK) with project 123F293. In this study, the photometric observations obtained within the scope of project numbered 12CT100-378 and 24BT100-2148, and carried out using the TUG100 telescope at the TUG site of the Türkiye National Observatories have been utilized; we express our gratitude for the support provided by the Türkiye National Observatories, the observation team and all its staff. Some of the data in this study were obtained with the T80 telescope at the Ankara University Astronomy and Space Sciences Research and Application Center (Kreiken Observatory) with project numbers 23B.T80.06 and 25BT80.01. We thank all the observers who report their observations to ETD and AXA open data bases. This work includes data collected with the TESS mission, obtained from the MAST data archive at the Space Telescope Science Institute (STScI). Funding for the TESS mission is provided by the NASA Explorer Program. STScI is operated by the Association of Universities for Research in Astronomy, Inc., under NASA contract NAS 5–26555. The authors acknowledge the use of public TESS data from pipelines at the TESS Science Office and at the TESS Science Processing Operations Center. Resources supporting this work were provided by the NASA High-End Computing (HEC) Program through the NASA Advanced Supercomputing (NAS) Division at Ames Research Center for the production of the SPOC data products. The authors acknowledge the use of the 2.2 m Telescope at the ESO Observatory in La Silla (Chile) and the use of the GROND camera, which was built by the high-energy group of MPE in collaboration with the LSW Tautenburg and ESO. We acknowledge the use of the Danish 1.54 m telescope at the ESO La Silla Observatory, within the framework of the MiNDSTEp consortium. The authors acknowledge the use of the Cassini 1.52 m Telescope operated by INAF-OAS (Astrophysics and Space Science Observatory of Bologna) in Loiano. The authors thank Ivan Bruni and Roberto Gualandi for their technical assistance at the Loiano Observatory. A.C.K. gratefully acknowledges the financial support of the TÜBİTAK 2210 National Graduate Scholarship no. 1649B022401264, UK Science and Technology Facilities Council (STFC) and the Faculty of Natural Sciences, Keele University in the form of a PhD studentship. A.J.B. was supported by STFC grants ST/W000873/1 and UKRI1179. L.M. acknowledges support from the MIUR-PRIN project no. 2022J4H55R. JS acknowledges support from STFC under grant No. ST/Y002563/1. S.A. acknowledges the funding from the Scientific Research Projects Coordination Unit of Istanbul University with the project number: FBA-2022-39121. IST60 telescope and its equipment are supported by the Republic of Turkey Ministry of Development (2016K12137) and Istanbul University with the project numbers BAP-3685, FBG-2017- 23943. A.Ö. acknowledges TÜBİTAK BİDEB for the support in terms of 2210 program. L.M. acknowledges financial contribution from PRIN MUR 2022 project 2022J4H55R. The work presented here is supported by the Carlsberg Foundation, grant CF25-0040. R.J.F.J. acknowledges the support provided by the GEMINI/ANID project under grant No. 32240028, by ANID’s Millennium Science Initiative through grant ICN12_009, awarded to the Millennium Institute of Astrophysics (MAS), and by ANID’s Basal project FB210003.

Author Contributions

A.C.K. wrote the paper, carried out all the calculations based on the TTV analysis results, and worked on the MESA models, Ö.B. organized the observations in Türkiye and the study, provided all the required codes for data manipulation and TTV analysis, contributed to the writing of the paper, and commented on the results,

A.B. contributed significantly to the stellar model and tidal computations and their interpretation, and edited the text of the manuscript,

S.Y. contributed to transit light curve modeling and the computation of the noise indicators as well as the error analysis,

J.S. organized the observations in La Silla, their reduction, and provided the required codes for data preparation, contributed significantly to the writing of the paper in terms of both grammar and scientific content,

S.O.S. was the PI of the project (123F293), contributed significantly to the target selection, organization as well as the writing of the paper in terms of its scientific content,

Student authors from Turkey (Ö.Z., K.K., F.A., İ.A.E., Z.Z., E.A., V.Ö., Ö.Y., D.İ., B.D., A.Ö., U.U., E.S.B., U.A., Y.T., S.H.) collected the light curves and mid-transit times, prepared the data for analysis, analyzed the light curves with the EXOFAST, and derived mid-transit timings of a particular target. Their order in the authors list depended on the volume of the data they analyzed,

L.M. organized the observations and reduced the data from Loiano and CAHA Observatories,

A.W. organized the observations and reduced the data from El Sauce Observatory,

F.T. and C.T.T. organized and carried out the observations and reduced the data from ATA50 Telescope,

S.A. and F.K.Y. organized and carried out the observations and reduced the data from IST60 Telescope,

MiNDSTEp Team Members (M.J.B., R.F.C., R.J.F.J., T.C. H., V.O., J.T.-R.) funded the operation of the DK154 telescope, carried out the observations, performed photometric data reduction, and contributed to the final draft of the manuscript.

Facilities: La Silla (DK154–Danish 1.54m Telescope, GROND–Max Planck:2.2m, NTT), Loiano–1.52m (BFOSC).

Software: astropy (Astropy Collaboration et al. 2013, 2018, 2022), AstroImageJ (Collins et al. 2017b), EXOFAST (Eastman et al. 2013), matplotlib (Hunter 2007), MESA (Paxton et al. 2011, 2013, 2015, 2018, 2019; Jermyn et al. 2023), numpy (C. Harris et al. 2020), pandas (T. pandas development team 2020), pymc (Abril-Pla et al. 2023), scipy (Virtanen et al. 2020).

Appendix
Additional Tables

We provide additional information on the dataset of light curves that we used throughout the study. In Table A1, we present the TESS sectors included in this work. Table A2 and

Table A1
Analyzed TESS Sectors for Systems in Our Sample

System	TESS Sector
CoRoT-2	54, 81
HAT-P-23	54, 55, 81
HATS-18	10, 36, 63, 90
KELT-9	14, 15, 41, 55, 75, 82
KELT-16	15, 41, 55
Qatar-1	17, 24, 41, 48, 51, 55, 56, 57, 59, 75, 76, 77, 78, 82, 83, 84, 85, 86
Qatar-4	57, 84
TOI-2109	52, 79
TOI-1937A	34, 35, 36, 61, 62, 88, 89
TrEs-1	14, 41, 53, 54, 74, 80
WASP-3	26, 40, 53, 54, 74, 80, 81
WASP-12	20, 43, 44, 45, 71, 72
WASP-19	9, 36, 62, 63, 89, 90
WASP-46	1, 27, 67
WASP-87	10, 11, 37
WASP-103	…
WASP-114	55, 82
WASP-121	7, 33, 34, 61, 87, 88
WASP-122	7, 33, 34, 61, 87, 88
WASP-167	10, 37, 64

Table A2
Number of Light Curves Analysed and Minimum Adopted from the Literature Sources for each Planetary System in Our Sample

Planet	ETD	L_1	L_2	TESS	Ours	T
CoRoT-2 b	38	33	86	18	0	175
HAT-P-23 b	28	32	13	56	1	130
HATS-18 b	4	2	28	105	2	141
KELT-9 b	0	8	23	94	0	125
KELT-16 b	15	0	60	60	0	135
Qatar-1 b	322	12	65	302	11	712
Qatar-4 b	32	1	1	24	1	59
TOI-2109 b	0	11	23	47	3	84
TOI-1937A b	0	0	6	168	0	174
TrES-1 b	14	42	7	39	1	103
WASP-3 b	68	19	56	79	3	212
WASP-12 b	83	0	78	116	2	279
WASP-19 b	50	31	36	174	10	301
WASP-46 b	33	0	22	45	0	100
WASP-87 b	3	0	7	37	0	47
WASP-103 b	8	82	0	0	2	92
WASP-114 b	11	2	0	24	2	39
WASP-121 b	9	17	0	105	4	135
WASP-122 b	9	0	4	78	0	91
WASP-167 b	5	0	5	32	0	42
Total	732	292	520	1603	42	3188

Note. L_1 is the number of adopted minima times from the literature sources, L_2 is the light curve number originated from literature and analysed using AIJ and EXOFAST, and T is the total number of minimum times.

Table A3
Same as **Table** A2 But After Selection Criterion Applied on the Dataset

Planet	ETD	L_1	L_2	TESS	Ours	T
CoRoT-2 b	30	33	80	14	0	153
HAT-P-23 b	25	32	13	55	1	126
HATS-18 b	4	2	28	102	2	138
KELT-9 b	0	8	23	94	0	125
KELT-16 b	7	0	36	53	0	96
Qatar-1 b	304	12	65	302	10	693
Qatar-4 b	29	1	1	23	1	55
TOI-2109 b	0	11	15	45	0	71
TOI-1937A b	0	0	5	156	0	161
TrEs-1 b	10	42	6	37	1	96
WASP-3 b	53	19	52	77	3	204
WASP-12 b	49	0	69	113	2	233
WASP-19 b	48	31	33	171	7	290
WASP-46 b	26	0	17	45	0	88
WASP-87 b	0	0	3	21	0	24
WASP-103 b	8	82	0	0	2	92
WASP-114 b	9	2	0	20	2	33
WASP-121 b	3	17	0	103	4	127
WASP-122 b	4	0	4	77	0	85
WASP-167 b	3	0	5	28	0	36
Total	612	292	455	1536	35	2930

Table A4
Mid-transit Times We Derived from the Light Curves in the Exoplanet Transit Database (ETD) ($T_{0,\mathrm{cal}}$), Their Uncertainties (σ), Mid-transit Times Reported by the Observers of ETD from the Same Light Curves $T_{0,\mathrm{ref}}$

System	Observer	Filter	$T_{0,\mathrm{ref}}$	$T_{0,\mathrm{cal}}$	σ	omit?	β	PNR	Comments
CoRoT-2	Yves Jongen	clear	2460559.386569	2460559.387443	0.000362	0	1.924	1.546	
CoRoT-2	Yves Jongen	clear	2460067.861817	2460067.861979	0.000254	0	2.291	1.252	
CoRoT-2	Yves Jongen	clear	2459431.668172	2459431.668660	0.000292	0	2.141	1.372	
CoRoT-2	Yves Jongen	clear	2459412.495652	2459412.496588	0.000460	0	1.444	2.103	
...	...	...	...	...	...	...	...	...	...

Table A5
Mid-transit Times We Adopted from Previous Works

System	Source	$T_{0,\mathrm{ref}}$	σ_{ref}
CoRoT-2	Bouchy et al. (2008)	2454237.536	0.00014
CoRoT-2	Rauer et al. (2009); Adams et al. (2024)	2454624.481	0.0016
CoRoT-2	Rauer et al. (2009); Adams et al. (2024)	2454676.762	0.0008
CoRoT-2	Rauer et al. (2009); Adams et al. (2024)	2454678.502	0.0012
CoRoT-2	Rauer et al. (2009); Adams et al. (2024)	2454683.741	0.0014
...	...	...	...

Note. Note That We Provide the Bibcode of the Study in the CDS Version of this Table.

Table A6

Mid-transit Times We Derived from the Light Curves in the Previous Studies ($T_{0,\mathrm{cal}}$), Their Uncertainties (σ_{cal}), Mid-transit Times Reported in the Corresponding Study ($T_{0,\mathrm{ref}}$) and Their Uncertainties (σ_{ref})

System	Source	$T_{0,\mathrm{ref}}$	σ_{ref}	$T_{0,cal}$	σ_{cal}	β	PNR	Comments
CoRoT-2	Adams et al. (2024)	2454237.534500	0.0017	2454237.535189	0.000265	2.972	0.273	Beta criteria
CoRoT-2	Adams et al. (2024)	2454239.278590	0.00029	2454239.278895	0.000251	1.628	3.377	
CoRoT-2	Adams et al. (2024)	2454241.022200	0.00024	2454241.022116	0.000271	1.525	3.382	
CoRoT-2	Adams et al. (2024)	2454242.765440	0.00025	2454242.765626	0.000161	1.539	3.119	
CoRoT-2	Adams et al. (2024)	2454244.508370	0.00025	2454244.508497	0.000193	1.458	2.924	
...	...	...	...	...	...	...	...	...

Note. Note that we provide the bibcode of the study in the CDS version of this table.

Table A7

Mid-transit Times We Derived from the TESS Light Curves ($T_{0,\mathrm{cal}}$), Their Uncertainties (σ_{cal})

System	$T_{0,cal}$	σ_{cal}	β	*PNR*	Comments
CoRoT-2	2459771.551759	0.000381	1.944	2.361	
CoRoT-2	2459773.294693	0.000399	2.211	2.334	
CoRoT-2	2459783.753239	0.000428	2.528	2.589	Beta criteria
CoRoT-2	2459785.495646	0.000404	1.959	2.365	
CoRoT-2	2459787.238485	0.000421	2.134	2.410	
…	…	…	…	…	…

Table A8

Adopted Ephemeris Information of Our Sample in this Study

Planet	T_0 ($\mathrm{BJD_{TDB}}$)	P_{orb} (days)	References
CoRoT-2 b	2457683.44158(16)	1.74299705(15)	(1)
HAT-P-23 b	2457742.573790(72)	1.212886397(74)	(1)
HATS-18 b	2458626.51102(45)	0.83784369(11)	(2)
KELT-9 b	2457095.68572(14)	1.4811235(11)	(3)
KELT-16 b	2458392.597691(78)	0.968992962(97)	(4)
Qatar-1 b	2456234.103218(60)	1.42002420(22)	(5)
Qatar-4 b	2457637.77361(46)	1.805356400(1)	(6)
TOI-2109 b	2459378.459370(59)	0.672474140(28)	(7)
TOI-1937A b	2459085.91023(7)	0.94667944(9)	…
TrES-1 b	2456822.891157(63)	3.030069476(72)	(1)
WASP-3 b	2454143.85112(24)	1.84683510(40)	(8)
WASP-12 b	2457010.512173(70)	1.091419108(55)	(9)
WASP-19 b	2456885.482836(37)	0.788839092(24)	(1)
WASP-46 b	2455392.31659(58)	1.43036763(93)	(10)
WASP-87 b	2458276.86087(15)	1.68279422(22)	(1)
WASP-103 b	2457308.324538(30)	0.925545386(56)	(1)
WASP-114 b	2457522.66047(24)	1.54877501(34)	(1)
WASP-121 b	2458119.72074(17)	1.27492504(15)	(12)
WASP-122 b	2456665.22401(21)	1.7100566(32)	(13)
WASP-167 b	2458117.02169(19)	2.02195933(33)	(1)

References: 1. Kokori et al. (2023), 2. Southworth et al. (2022), 3. Gaudi et al. (2017), 4. Oberst et al. (2017), 5. Collins et al. (2017a), 6. Alsubai et al. (2017), 7. Wong et al. (2021), 8. Bonomo et al. (2017), 9. Ivshina & Winn (2022), 10. Ciceri et al. (2016), 11. Addison et al. (2016), 12. Bourrier et al. (2020), 13. Turner et al. (2016).

Table A9

Median-fit Results from Our Apsidal Motion Models for the HJs with $e > 0$, Compared with the Linear Model Presented in Table 4

System	ΔBIC	e $(\times 10^{-3})$	ω (rad)	ωdE $(\times 10^{-4\circ}/\text{cycle})$
CoRoT-2	3021.216	$1.01^{+0.19}_{-0.31}$	$1.96^{+0.11}_{-0.14}$	$17.47^{+2.59}_{-2.70}$
HAT-P-23	688.66	$1.49^{+0.967}_{-1.18}$	$3.14^{+1.78}_{-1.79}$	$5.81^{+5.75}_{-5.63}$
HATS-18	457.149	$1.106^{+0.770}_{-1.382}$	$2.70^{+1.78}_{-2.32}$	$3.28^{+4.88}_{-5.98}$
KELT-9	215.01	$0.301^{+0.148}_{-0.301}$	$2.90^{+0.64}_{-0.82}$	$15.3^{+3.03}_{-3.04}$
WASP-3	472.06	$0.55^{+0.30}_{-0.56}$	$1.73^{+0.940}_{-1.27}$	$372.7^{+101.2}_{-105.5}$
WASP-19	> 5000	$3.4991^{+0.0014}_{-0.0006}$	$3.28^{+3.07}_{-3.00}$	$1182.413^{+7.192}_{-6.799}$
TOI-2109	187.26	$1.70^{+1.09}_{-1.20}$	$3.15^{+1.99}_{-2.00}$	$5.74^{+5.69}_{-5.75}$
WASP-114	146.95	$1.392^{+0.904}_{-1.223}$	$3.09^{+2.16}_{-2.25}$	$5.71^{+5.71}_{-5.72}$
WASP-167	765.9	$2.68^{+0.91}_{-0.58}$	$3.26^{+0.69}_{-0.62}$	$5.83^{+5.74}_{-5.76}$

A3 present the number of light curves modelled for each object in our sample. For Table A4, A5, A6 and A7, the full table is available at the CDS table.

ORCID iDs

Ahmet Cem Kutluay https://orcid.org/0009-0007-0502-7359
Özgür Baştürk https://orcid.org/0000-0002-4746-0181
Adrian J. Barker https://orcid.org/0000-0003-4397-7332
Selçuk Yalçınkaya https://orcid.org/0000-0002-5224-247X
John Southworth https://orcid.org/0000-0002-3807-3198
Selim Osman Selam https://orcid.org/0000-0002-4953-4818
Özlem Şimşir https://orcid.org/0009-0007-8172-6602
Kaan Kaplan https://orcid.org/0000-0003-0631-1961
Furkan Akar https://orcid.org/0000-0003-4419-2908
İpek Aleyna Ertürk https://orcid.org/0009-0000-8026-2104
Zeynep Zengin https://orcid.org/0009-0002-8061-8857
Ebrar Akalın https://orcid.org/0009-0009-5717-5382
Volkan Özsoy https://orcid.org/0009-0001-8728-9200
Özdenur Yaldır https://orcid.org/0009-0007-6688-5584
Dilara İçöz https://orcid.org/0009-0008-2515-5830
Luigi Mancini https://orcid.org/0000-0002-9428-8732
Burak Duru https://orcid.org/0009-0003-2191-8873
Fatma Tezcan https://orcid.org/0000-0001-5715-1166
Alkım Özfidan https://orcid.org/0009-0007-9111-5629
Ushna Umar https://orcid.org/0009-0007-6246-0933
Anaël Wünsche https://orcid.org/0000-0002-6176-9847
Martin J. Burgdorf https://orcid.org/0000-0002-5854-4217
Richard E. Cannon https://orcid.org/0009-0007-5946-8731
Roberto Jose Figuera Jaimes https://orcid.org/0000-0003-3425-6605
Tobias Cornelius Hinse https://orcid.org/0000-0001-8870-3146
Jeremy Tregloan-Reed https://orcid.org/0000-0002-9024-4185
Elif Sıla Buğday https://orcid.org/0009-0007-5714-2391
Utku Akdere https://orcid.org/0009-0001-3015-7426
Yiğit Turan https://orcid.org/0009-0003-9028-3584
Sinan Aliş https://orcid.org/0000-0002-6990-8899
Cihan Tuğrul Tezcan https://orcid.org/0000-0003-2253-9499
Fuat Korhan Yelkenci https://orcid.org/0000-0003-2675-3564

References

Abril-Pla, O., Andreani, V., Carroll, C., et al. 2023, PeerJ Computer Science, 9, e1516
Adams, E. R., Jackson, B., & Amanda, A. S. 2024, PSJ, 5, 163
Addison, B. C., Tinney, C. G., Wright, D. J., & Bayliss, D. 2016, ApJ, 823, 29
Agol, E., Steffen, J., Sari, R., & Clarkson, W. 2005, MNRAS, 359, 567
Ahlers, J. P., Johnson, M. C., Stassun, K. G., et al. 2020, AJ, 160, 4
Ahuir, J., Mathis, S., & Amard, L. 2021, A&A, 651, A3
Akaike, H. 1974, ITAC, 19, 716
Alonso, R., Auvergne, M., Baglin, A., et al. 2008, A&A, 482, L21
Alonso, R., Brown, T. M., Torres, G., et al. 2004, ApJL, 613, L153
Alsubai, K., Mislis, D., Tsvetanov, Z. I., et al. 2017, AJ, 153, 200
Alsubai, K. A., Parley, N. R., Bramich, D. M., et al. 2011, MNRAS, 417, 709
Alvarado, E., Bostow, K. B., Patra, K. C., et al. 2024, MNRAS, 534, 800
Anderson, D. R., Brown, D. J. A., Collier Cameron, A., et al. 2014, arXiv:1410.3449
Anderson, D. R., Collier Cameron, A., Gillon, M., et al. 2012, MNRAS, 422, 1988
Astoul, A., & Barker, A. J. 2023, ApJL, 955, L23
Astropy Collaboration, Price-Whelan, A. M., Lim, P. L., et al. 2022, ApJ, 935, 167
Astropy Collaboration, Price-Whelan, A. M., Sipőz, B. M., et al. 2018, AJ, 156, 123
Astropy Collaboration, Robitaille, T. P., Tollerud, E. J., et al. 2013, A&A, 558, A33
Baştürk, Ö., Esmer, E. M., Yalçınkaya, S., et al. 2022, MNRAS, 512, 2062
Baştürk, Ö., Hinse, T. C., Özavcı, İ., Yörükoğlu, O., & Selam, O. 2015, ASPC, 496, 370
Baştürk, Ö., Kutluay, A. C., Barker, A., et al. 2025, MNRAS, 541, 714
Bakos, G. Á., Hartman, J., Torres, G., et al. 2011, ApJ, 742, 116
Baluev, R. V., Sokov, E. N., Shaidulin, V. S., et al. 2015, MNRAS, 450, 3101
Barker, A. J. 2011, MNRAS, 414, 1365
Barker, A. J. 2020, MNRAS, 498, 2270
Barker, A. J. 2025, arXiv:2504.10941
Barker, A. J., Efroimsky, M., Makarov, V. V., & Veras, D. 2024, MNRAS, 527, 5131
Barker, A. J., & Ogilvie, G. I. 2009, MNRAS, 395, 2268
Barker, A. J., & Ogilvie, G. I. 2010, MNRAS, 404, 1849
Barnes, S. A., Weingrill, J., Fritzewski, D., Strassmeier, K. G., & Platais, I. 2016, ApJ, 823, 16

Barros, S. C. C., Akinsanmi, B., Boué, G., et al. 2022, A&A, 657, A52
Barros, S. C. C., Brown, D. J. A., Hébrard, G., et al. 2016, A&A, 593, A113
Biagiotti, F., Mancini, L., Southworth, J., et al. 2024, A&A, 685, A131
Birkby, J. L., Cappetta, M., Cruz, P., et al. 2014, MNRAS, 440, 1470
Biswas, S., Bisht, D., & Jiang, I.-G. 2024, 8th TESS/15th Kepler Asteroseismic Science Consortium Workshop, v1, Zenodo, doi:10.5281/zenodo.13681422
Bonomo, A. S., Desidera, S., Benatti, S., et al. 2017, A&A, 602, A107
Bouchy, F., Queloz, D., Deleuil, M., et al. 2008, A&A, 482, L25
Bouma, L. G., Winn, J. N., Baxter, C., et al. 2019, AJ, 157, 217
Bourrier, V., Ehrenreich, D., Lendl, M., et al. 2020, A&A, 635, A205
Bruno, G., Deleuil, M., Almenara, J. M., et al. 2016, A&A, 595, A89
Buzzoni, B., Delabre, B., Dekker, H., et al. 1984, Msngr, 38, 9
Cauley, P. W., Redfield, S., & Jensen, A. G. 2017, AJ, 153, 81
Chernov, S. V., Ivanov, P. B., & Papaloizou, J. C. B. 2017, MNRAS, 470, 2054
Choi, J., Dotter, A., Conroy, C., et al. 2016, ApJ, 823, 102
Chontos, A., Huber, D., Latham, D. W., et al. 2019, AJ, 157, 192
Christiansen, J. L., McElroy, D. L., Harbut, M., et al. 2025, PSJ, 6, 186
Ciceri, S., Mancini, L., Southworth, J., et al. 2013, A&A, 557, A30
Ciceri, S., Mancini, L., Southworth, J., et al. 2015, A&A, 577, A54
Ciceri, S., Mancini, L., Southworth, J., et al. 2016, MNRAS, 456, 990
Claret, A., & Bloemen, S. 2011, A&A, 529, A75
Claret, A., & Gimenez, A. 1989, A&AS, 81, 37
Collins, K. A., Kielkopf, J. F., & Stassun, K. G. 2017a, AJ, 153, 78
Collins, K. A., Kielkopf, J. F., Stassun, K. G., & Hessman, F. V. 2017b, AJ, 153, 77
Cortés-Zuleta, P., Rojo, P., Wang, S., et al. 2020, A&A, 636, A98
Covino, E., Esposito, M., Barbieri, M., et al. 2013, A&A, 554, A28
Damiani, C., & Lanza, A. F. 2015, A&A, 574, A39
De, K., MacLeod, M., Karambelkar, V., et al. 2023, Natur, 617, 55
Delrez, L., Santerne, A., Almenara, J. M., et al. 2016, MNRAS, 458, 4025
Dominik, M., Jørgensen, U. G., Rattenbury, N. J., et al. 2010, AN, 331, 671
Dotter, A. 2016, ApJS, 222, 8
Duguid, C. D., Barker, A. J., & Jones, C. A. 2020, MNRAS, 497, 3400
Duguid, C. D., de Vries, N. B., Lecoanet, D., & Barker, A. J. 2024, ApJL, 966, L14
Eastman, J., Gaudi, B. S., & Agol, E. 2013, PASP, 125, 83
Eastman, J., Siverd, R., & Gaudi, B. S. 2010, PASP, 122, 935
Eibe, M. T., Cuesta, L., Ullán, A., Pérez-Verde, A., & Navas, J. 2012, MNRAS, 423, 1381
Esposito, M., Covino, E., Desidera, S., et al. 2017, A&A, 601, A53
Esseldeurs, M., Mathis, S., & Decin, L. 2024, A&A, 690, A266
Essick, R., & Weinberg, N. N. 2016, ApJ, 816, 18
Fossati, L., Haswell, C. A., Froning, C. S., et al. 2010, ApJL, 714, L222
Fulton, B. J., Shporer, A., Winn, J. N., et al. 2011, AJ, 142, 84
Gallet, F., Bolmont, E., Mathis, S., et al. 2017, A&A, 604, A112
Garhart, E., Deming, D., Mandell, A., et al. 2020, AJ, 159, 137
Gaudi, B. S., Stassun, K. G., Collins, K. A., et al. 2017, Natur, 546, 514
Gillon, M., Lanotte, A. A., Barman, T., et al. 2010, A&A, 511, A3
Gillon, M., Anderson, D. R., Collier-Cameron, A., et al. 2014, A&A, 562, L3
Goldreich, P., & Soter, S. 1966, Icar, 5, 375
Goodman, J., & Dickson, E. S. 1998, ApJ, 507, 938
Greiner, J., Bornemann, W., Clemens, C., et al. 2008, PASP, 120, 405
Griffiths, A. W., Southworth, J., Alegre, L., et al. 2026, MNRAS, 545, staf2057
Gu, P.-G., Lin, D. N. C., & Bodenheimer, P. H. 2003, ApJ, 588, 509
Guillot, T., Burrows, A., Hubbard, W. B., Lunine, J. I., & Saumon, D. 1996, ApJL, 459, L35
Guo, Z., Ogilvie, G. I., & Barker, A. J. 2023, MNRAS, 521, 1353
Hagey, S. R., Edwards, B., & Boley, A. C. 2022, AJ, 164, 220
Hagey, S. R., Edwards, B., Tsiaras, A., et al. 2025, AJ, 170, 197
Hamer, J. H., & Schlaufman, K. C. 2019, AJ, 158, 190
Hamer, J. H., & Schlaufman, K. C. 2020, AJ, 160, 138
Harre, J. V., Smith, A. M. S., Barros, S. C. C., et al. 2023, A&A, 669, A124
Harre, J.-V., Smith, A. M. S., Barros, S. C. C., et al. 2024, A&A, 692, A254
Harris, C., Millman, K. J., van der Walt, S. J., et al. 2020, Natur, 585, 357
Hebb, L., Collier-Cameron, A., Loeillet, B., et al. 2009, ApJ, 693, 1920
Hebb, L., Collier-Cameron, A., Triaud, A. H. M. J., et al. 2010, AJ, 708, 224
Hellier, C., Anderson, D. R., Collier Cameron, A., et al. 2009, Natur, 460, 1098
Hellier, C., Anderson, D. R., Collier Cameron, A., et al. 2011, A&A, 535, L7
Hiltner, W. A. 1962, Astronomical techniques (Univ. of Chicago Press)
Hoeijmakers, H. J., Ehrenreich, D., Kitzmann, D., et al. 2019, A&A, 627, A165
Honeycutt, R. K. 1992, PASP, 104, 435
Hoyer, S., Pallé, E., Dragomir, D., & Murgas, F. 2016, AJ, 151, 137
Hroch, F. 2014, Munipack: General astronomical image processing software, Astrophysics Source Code Library, ascl: 1402.006
Hunter, J. D. 2007, CSE, 9, 90
Hut, P. 1980, A&A, 92, 167
Hut, P. 1981, A&A, 99, 126
Ivshina, E. S., & Winn, J. N. 2022, ApJS, 259, 62
Jackson, B., Adams, E. R., & Morgenthaler, J. P. 2023, AJ, 166, 142
Jankowski, A. R., Becker, J., Soares-Furtado, M., Vanderburg, A., & He, Z. 2025, PASP, 137, 034401
Jenkins, J. M., Twicken, J. D., McCauliff, S., et al. 2016, SPIE, 9913, 99133E
Jermyn, A. S., Bauer, E. B., Schwab, J., et al. 2023, ApJS, 265, 15
Jones, K., Morris, B. M., Demory, B.-O., et al. 2022, A&A, 666, A118
Kálmán, S., Derekas, A., Csizmadia, S., et al. 2024, A&A, 687, A144
Knutson, H. A., Fulton, B. J., Montet, B. T., et al. 2014, ApJ, 785, 126
Kokori, A., Tsiaras, A., Edwards, B., et al. 2022, ApJS, 258, 40
Kokori, A., Tsiaras, A., Edwards, B., et al. 2023, ApJS, 265, 4
Korth, J., & Parviainen, H. 2023, Univ, 10, 12
Kutluay, A. C., Basturk, O., Yalçinkaya, S., Saguner Rambaldi, T., & Yerli, S. K. 2023, TJAA, 4, 10
Lanza, A. F. 2020, MNRAS, 497, 3911
Lau, R. M., Jencson, J. E., Salyk, C., et al. 2025, ApJ, 983, 87
Lazovik, Y. A. 2021, MNRAS, 508, 3408
Lazovik, Y. A., Barker, A. J., de Vries, N. B., & Astoul, A. 2024, MNRAS, 527, 8245
Leonardi, P., Nascimbeni, V., Granata, V., et al. 2024, A&A, 686, A84
Levrard, B., Winisdoerffer, C., & Chabrier, G. 2009, ApJL, 692, L9
Liddle, A. R. 2007, MNRAS, 377, L74
Lightkurve Collaboration, Cardoso, J. V. d. M., Hedges, C., et al. 2018, Lightkurve: Kepler and TESS time series analysis in Python, Astrophysics Source Code Library, ascl: 1812.013
Lomb, N. R. 1976, Ap&SS, 39, 447
Ma, L., & Fuller, J. 2021, ApJ, 918, 16
Maciejewski, G. 2022, AcA, 72, 1
Maciejewski, G., Golonka, J., Fernández, M., et al. 2024, A&A, 692, A35
Maciejewski, G., Stangret, M., Ohlert, J., et al. 2018a, IBVS, 6243, 1
Maciejewski, G., Dimitrov, D., Neuhäuser, R., et al. 2010, MNRAS, 407, 2625
Maciejewski, G., Niedzielski, A., Wolszczan, A., et al. 2013, AJ, 146, 147
Maciejewski, G., Fernández, M., Aceituno, F. J., et al. 2015, A&A, 577, A109
Maciejewski, G., Dimitrov, D., Fernández, M., et al. 2016, A&A, 588, L6
Maciejewski, G., Fernández, M., Aceituno, F., et al. 2018b, AcA, 68, 371
Maciejewski, G., Fernández, M., Sota, A., et al. 2022, A&A, 667, A127
Mallonn, M., von Essen, C., Herrero, E., et al. 2019, A&A, 622, A81
Mancini, L., Giordano, M., Mollière, P., et al. 2016a, MNRAS, 461, 1053
Mancini, L., Kemmer, J., Southworth, J., et al. 2016b, MNRAS, 459, 1393
Mancini, L., Ciceri, S., Chen, G., et al. 2013a, MNRAS, 436, 2
Mancini, L., Southworth, J., Ciceri, S., et al. 2013b, A&A, 551, A11
Mancini, L., Southworth, J., Ciceri, S., et al. 2014a, MNRAS, 443, 2391
Mancini, L., Southworth, J., Ciceri, S., et al. 2014b, A&A, 562, A126
Mancini, L., Southworth, J., Raia, G., et al. 2017, MNRAS, 465, 843
Mancini, L., Southworth, J., Naponiello, L., et al. 2022, MNRAS, 509, 1447
Mannaday, V. K., Thakur, P., Southworth, J., et al. 2022, AJ, 164, 198
Mathis, S. 2015, A&A, 580, L3
Matsumura, S., Peale, S. J., & Rasio, F. A. 2010, ApJ, 725, 1995
McQuillan, A., Mazeh, T., & Aigrain, S. 2013, ApJL, 775, L11
Michel, K.-U., & Mugrauer, M. 2024, MNRAS, 527, 3183
Mohler-Fischer, M., Mancini, L., Hartman, J. D., et al. 2013, A&A, 558, A55
Montalto, M., Gregorio, J., Boué, G., et al. 2012, MNRAS, 427, 2757
Moutou, C., Díaz, R. F., Udry, S., et al. 2011, A&A, 533, A113
Mustill, A. J., Lambrechts, M., & Davies, M. B. 2021, in Cold Kinematics, PLATO Mission Conference 2021, 7
Nascimbeni, V., Cunial, A., Murabito, S., et al. 2013, A&A, 549, A30
Nascimbeni, V., Piotto, G., Cabrera, J., et al. 2025, A&A, 694, A313
Newville, M., Stensitzki, T., Allen, D. B., et al. 2016, Lmfit: Non-Linear Least-Square Minimization and Curve-Fitting for Python, Astrophysics Source Code Library, ascl: 1606.014

Nielsen, L. D., Brahm, R., Bouchy, F., et al. 2020, A&A, 639, A76
Oberst, T. E., Rodriguez, J. E., Colón, K. D., et al. 2017, AJ, 153, 97
Ogilvie, G. I. 2013, MNRAS, 429, 613
Ogilvie, G. I. 2014, ARA&A, 52, 171
Ogilvie, G. I., & Lin, D. N. C. 2007, ApJ, 661, 1180
O'Rourke, J. G., Knutson, H. A., Zhao, M., et al. 2014, ApJ, 781, 109
Öztürk, O., & Erdem, A. 2019, MNRAS, 486, 2290
T. pandas development team 2020, pandas-dev/pandas: Pandas, latest Zenodo: v3.0.1, Zenodo, doi:10.5281/zenodo.3509134
Patra, K. C., Winn, J. N., Holman, M. J., et al. 2017, AJ, 154, 4
Patra, K. C., Winn, J. N., Holman, M. J., et al. 2020, AJ, 159, 150
Paxton, B., Bildsten, L., Dotter, A., et al. 2011, ApJS, 192, 3
Paxton, B., Cantiello, M., Arras, P., et al. 2013, ApJS, 208, 4
Paxton, B., Marchant, P., Schwab, J., et al. 2015, ApJS, 220, 15
Paxton, B., Schwab, J., Bauer, E. B., et al. 2018, ApJS, 234, 34
Paxton, B., Smolec, R., Schwab, J., et al. 2019, ApJS, 243, 10
Penev, K. 2026, Encyclopedia of Astrophysics, Volume 1, Vol. 1 (Elsevier), 510
Penev, K., Bouma, L. G., Winn, J. N., & Hartman, J. D. 2018, AJ, 155, 165
Penev, K., & Sasselov, D. 2011, ApJ, 731, 67
Penev, K., Hartman, J. D., Bakos, G. Á., et al. 2016, AJ, 152, 127
Petrucci, R., Jofré, E., Ferrero, L. V., et al. 2018, MNRAS, 473, 5126
Petrucci, R., Jofré, E., Gómez Maqueo Chew, Y., et al. 2020, MNRAS, 491, 1243
Plavchan, P., Barclay, T., Gagné, J., et al. 2020, Natur, 582, 497
Poddaný, S., Brát, L., & Pejcha, O. 2010, NewA, 15, 297
Pollacco, D., Skillen, I., Collier Cameron, A., et al. 2008, MNRAS, 385, 1576
Pont, F. 2009, MNRAS, 396, 1789
Rabus, M., Deeg, H. J., Alonso, R., Belmonte, J. A., & Almenara, J. M. 2009a, A&A, 508, 1011
Rabus, M., Alonso, R., Belmonte, J. A., et al. 2009b, A&A, 494, 391
Raftery, A. E. 1995, Sociological Methodology, 25, 111, http://www.jstor.org/stable/271063
Rauer, H., Erikson, A., Kabath, P., et al. 2009, AJ, 139, 53
Rauer, H., Aerts, C., Cabrera, J., et al. 2025, ExA, 59, 26
Rodriguez, J. E., Colón, K. D., Stassun, K. G., et al. 2016, AJ, 151, 138
Rosário, N. M., Barros, S. C. C., Demangeon, O. D. S., & Santos, N. C. 2022, A&A, 668, A114
Rostron, J. W., Wheatley, P. J., Anderson, D. R., et al. 2014, MNRAS, 441, 3666
Salisbury, M. A., Kolb, U. C., Norton, A. J., & Haswell, C. A. 2021, NewA, 83, 101477
Salz, M., Schneider, P. C., Fossati, L., et al. 2019, A&A, 623, A57
Scargle, J. D. 1982, ApJ, 263, 835
Schwarz, G. 1978, AnSta, 6, 461
Shan, S.-S., Yang, F., Lu, Y.-J., et al. 2023, ApJS, 264, 37
Shen, Y., & Turner, E. L. 2008, ApJ, 685, 553
Simpson, E. K., Pollacco, D., Hébrard, G., et al. 2010, MNRAS, 405, 1867
Sing, D. K., Evans-Soma, T. M., Rustamkulov, Z., et al. 2024, AJ, 168, 231
Siverd, R. J., Beatty, T. G., Pepper, J., et al. 2012, ApJ, 761, 123
Sodickson, N., & Grunblatt, S. 2025, ApJ, 993, 78
Southworth, J. 2011, MNRAS, 417, 2166
Southworth, J., Mancini, L., Madhusudhan, N., et al. 2017, AJ, 153, 191
Southworth, J., Hinse, T. C., Burgdorf, M. J., et al. 2009a, MNRAS, 399, 287
Southworth, J., Hinse, T. C., Jørgensen, U. G., et al. 2009b, MNRAS, 396, 1023
Southworth, J., Hinse, T. C., Burgdorf, M., et al. 2014, MNRAS, 444, 776
Southworth, J., Mancini, L., Ciceri, S., et al. 2015, MNRAS, 447, 711
Southworth, J., Barker, A. J., Hinse, T. C., et al. 2022, MNRAS, 515, 3212
Spalding, C., & Winn, J. N. 2022, ApJ, 927, 22
Stangret, M., Palle, E., Esparza-Borges, E., et al. 2024, A&A, 691, A120
Stassun, K. G., Collins, K. A., & Gaudi, B. S. 2017, AJ, 153, 136
Stephan, A. P., Wang, J., Cauley, P. W., et al. 2022, ApJ, 931, 111
Stetson, P. B. 1987, PASP, 99, 191
Su, L.-H., Jiang, I.-G., Sariya, D. P., et al. 2021, AJ, 161, 108
Temple, L. Y., Hellier, C., Albrow, M. D., et al. 2017, MNRAS, 471, 2743
Tingley, B., Endl, M., Gazzano, J. C., et al. 2011, A&A, 528, A97
Torres, G., Winn, J. N., & Holman, M. J. 2008, ApJ, 677, 1324
Tregloan-Reed, J., & Southworth, J. 2013, MNRAS, 431, 966
Tregloan-Reed, J., Southworth, J., & Tappert, C. 2013, MNRAS, 428, 3671
Turner, J. D., Flagg, L., Ridden-Harper, A., & Jayawardhana, R. 2022, AJ, 163, 281
Turner, J. D., Ridden-Harper, A., & Jayawardhana, R. 2021, AJ, 161, 72
Turner, O. D., Anderson, D. R., Collier Cameron, A., et al. 2016, PASP, 128, 064401
Valsecchi, F., & Rasio, F. A. 2014, ApJ, 786, 102
VanderPlas, J. T. 2018, ApJS, 236, 16
Virtanen, P., Gommers, R., Oliphant, T. E., et al. 2020, NatMe, 17, 261
von Essen, C., Schröter, S., Agol, E., & Schmitt, J. H. M. M. 2013, A&A, 555, A92
Wang, J., Fischer, D. A., Horch, E. P., & Huang, X. 2015, ApJ, 799, 229
Wang, W., Zhang, Z., Chen, Z., et al. 2024, ApJS, 270, 14
Weinberg, N. N., Arras, P., Quataert, E., & Burkart, J. 2012, ApJ, 751, 136
Weinberg, N. N., Davachi, N., Essick, R., et al. 2024, ApJ, 960, 50
Weinberg, N. N., Sun, M., Arras, P., & Essick, R. 2017, ApJL, 849, L11
Wilkins, A. N., Delrez, L., Barker, A. J., et al. 2017, ApJL, 836, L24
Winn, J. 2019, AAS/Division for Extreme Solar Systems Abstracts, 51, 201.04
Winn, J. N., Holman, M. J., Torres, G., et al. 2008, ApJ, 683, 1076
Wong, I., Shporer, A., Vissapragada, S., et al. 2022, AJ, 163, 175
Wong, I., Shporer, A., Kitzmann, D., et al. 2020, AJ, 160, 88
Wong, I., Shporer, A., Zhou, G., et al. 2021, AJ, 162, 256
Yan, D., Guo, J., Huang, C., & Xing, L. 2021, ApJL, 907, L47
Yee, S. W., Winn, J. N., Knutson, H. A., et al. 2020, ApJL, 888, L5
Yee, S. W., Winn, J. N., Hartman, J. D., et al. 2023, ApJS, 265, 32
Zahn, J. P. 1975, A&A, 41, 329
Zahn, J. P. 1977, A&A, 57, 383
Zak, J., Boffin, H. M. J., Sedaghati, E., et al. 2025, A&A, 694, A91
Zhou, G., Bakos, G. Á., Bayliss, D., et al. 2019, AJ, 157, 31